JOURNAL OF PETROLOGY | VOLUME 43 | NUMBER 2 | PAGES 243–270 | 2002

Magma Mixing and Crustal Recycling Recorded in Ternary Feldspar from Compositionally Zoned Peralkaline Ignimbrite 'A', Gran Canaria, Canary Islands

VALENTIN R. TROLL* AND HANS-ULRICH SCHMINCKE

ABTEILUNG FÜR VULKANOLOGIE UND PETROLOGIE, GEOMAR FORSCHUNGSZENTRUM DER CHRISTIAN-ALBRECHTS-UNIVERSITÄT ZU KIEL, WISCHHOFSTRAßE 1–3, 24148 KIEL, GERMANY

RECEIVED OCTOBER 25, 2000; REVISED TYPESCRIPT ACCEPTED AUGUST 10, 2001

Miocene Ignimbrite 'A' on Gran Canaria contains three compositional endmember fiamme types (two rhyolites and one trachyte) each of which crystallized distinct feldspar. Various textural and compositional criteria are interpreted as reflecting a complex scenario within the magma chamber in which the crystals formed. About 25–30% of the feldspar phenocrysts contain evidence for magma mixing in the form of (1) partial to severe dissolution–resorption rims, (2) distinct zones of drastically different compositions and (3) overgrowth textures on formerly resorbed crystals. Four major types of zoning in the oligoclase to anorthoclase feldspars of ignimbrite 'A' include a normal and a reversely zoned type and two complexly zoned types. The feldspars with normal and reverse zonation show only minor compositional amplitudes between individual zones (ΔAb, Or ∼4%), whereas the complexly zoned types show compositional differences between zones of up to 18 mol % Ab and 20 mol % Or and are commonly associated with an internal dissolution surface. Complex zoning with large compositional amplitudes and dissolution textures is taken as evidence of crystal movements within the magma and across compositional boundaries between magma batches. A multiple 'step-cycle' model, involving growth and transport of a crystal into another magma batch and its return to the original host magma, is suggested by the data. Moreover, feldspars from one rhyolite compositional group are found to be substantially elevated in $\delta^{18}O$, suggesting an input of a high $\delta^{18}O$ component to this rhyolite. The other endmember rhyolite appears to be related to the endmember trachyte by mainly crystal fractionation of anorthoclase feldspar. This observation is consistent with trace element and rare earth element concentrations for the magma endmembers and their feldspars, where contamination led to a depletion in incompatible trace elements and light rare earth elements in the contaminated rhyolite and its feldspar phenocrysts. We suggest that the combination of textural and compositional variation in ternary feldspar of peralkaline rhyolitic systems is well suited to reconstruct dynamic processes such as magma mixing and contamination in evolving rhyolitic magma chambers.

KEY WORDS: *ternary feldspar; peralkaline ignimbrites; ocean islands; Gran Canaria*

INTRODUCTION

Feldspar crystals in volcanic rocks record crystallization, magma mixing and contamination of their host magmas, partly because of slow diffusion of alkali elements in feldspar compared with the time scales of magmatic events. In basalts and calc-alkaline systems, compositional variations in feldspar have been used to interpret variations in the physical and chemical conditions brought about by processes such as magma mixing, pressure changes and convection during crystallization (e.g. Pearce & Kolisnik, 1990; Stamatelopoulou-Seymore *et al.*, 1990;

*Corresponding author. Present address: Department of Geology, Trinity College, Dublin 2, Ireland. Telephone: 00353-(0)1-608-3856. Fax: 00353-(0)1-671-1199. E-mail: trollv@tcd.ie

Blundy & Shimizu, 1991; Singer *et al.*, 1995; van Wagoner *et al.*, 1995; Brophy *et al.*, 1996; Davidson & Tepley, 1997; Knesel *et al.*, 1999; Tepley *et al.*, 1999; Davidson *et al.*, 2001; Stewart & Fowler, 2001). Similar studies of anorthoclase, the most common phenocryst in peralkaline trachytes and rhyolites (i.e. comendites and pantellerites), are uncommon, one reason being that compositional zoning is petrographically less pronounced.

On Gran Canaria, some 20 Miocene, dominantly peralkaline rhyolitic to trachytic ignimbritic cooling units (Mogan Group) contain the entire compositional range of anorthoclase compositions, with nearly albitic compositions at the base and almost sanidine compositions near the top of the stratigraphic succession (Schmincke, 1969, 1976; Sumita & Schmincke, 1998). All ignimbrites contain two or more magmatic endmembers as well as several feldspar compositional groups. The exact compositions of the magmatic endmembers are not easy to define because of common magma mixing, high-temperature devitrification and the problem of interpreting ignimbrite whole-rock compositions, glass inclusions and the very rare entirely fresh and undevitrified glass from basal vitrophyres. Feldspar phenocrysts that are basically unaffected by post-emplacement processes provide one expression of the complex petrogenetic processes the endmember magmas underwent before eruption.

We studied ternary feldspar phenocrysts from a peralkaline trachyte–rhyolite ignimbrite (ignimbrite 'A') of the Upper Mogan Group, to unravel the crystallization, mixing and contamination history of the unit, and to decode the textural and compositional variation of its crystal population. We show that three compositional feldspar groups are present and that these correspond to the three fiamme compositional groups of the ignimbrite, an endmember trachyte and two rhyolites. Compositional zoning in a sub-population of the feldspars in these rocks suggests that crystals were transferred between the compositionally distinct magma batches by a magma mixing process. One rhyolite magma composition appears to be related to the trachyte magma by mainly crystal fractionation, whereas the second rhyolite is believed to have been compositionally diluted as a result of input of a high $\delta^{18}O$ component that was low in incompatible trace and light rare earth elements (LREE).

METHODS

Approximately 120 samples were collected from several outcrops distributed over the south and the west of Gran Canaria (Fig. 1). Samples were prepared as powder for X-ray fluorescence (XRF) and as polished thin and doubly polished thick sections for optical microscopy, electron microprobe (EMP) and sychrotron-XRF microprobe (SYXRF) analysis. Mineral separates were hand-picked from crushed rock. The different types of analysis were performed on single samples by subdividision of the original sample into several batches, where one batch was powdered, another batch was prepared for thin and thick sections and yet another batch was crushed and picked for mineral separates.

Electron microprobe

Mineral analyses were performed on a Cameca SX-50 electron microprobe at GEOMAR applying the built-in PAP correction procedure (Pouchou & Pichoir, 1984). Analytical conditions included an acceleration voltage of 15 kV, a beam current of 8–20 nA, and counting times of between 20 and 60 s on peaks. A rastered beam of 3 μm × 4 μm (12 μm^2) was used for feldspar, and of ~40 μm^2 for glass to minimize Na loss. Na counts were continuously monitored during analysis and generally remained stable over at least twice the measurement time. Glass analyses were corrected for Na migration (Nielsen & Sigurdsson 1981; Devine *et al.*, 1995). Relative analytical precision [(standard deviation/mean) × 100] was <2% for Si, Al and Ca, <3% for Na and K, <4% for Ti, <5% for Fe, and <10% for Mg, based on repeated analysis of natural and synthetic mineral and glass standards.

X-ray fluorescence

Unweathered central pieces of the samples were cut and selected for whole-rock analysis, avoiding cracks and rims affected by alteration. Samples for whole-rock analyses were crushed and powdered in agate ball-mills. Samples were dried at 110°C before analysis. Major and trace elements were determined by XRF on fused beads using an automated Philips PW1480 spectrometer at GEOMAR. All analyses were performed with a Rh tube; calibration was performed using international geological reference samples.

Inductively coupled plasma-mass spectrometry

Trace elements and REE were analysed by inductively coupled plasma-mass spectrometry (ICPMS) on a Perkin Elmer Sciex ELAN 5000 at Actlabs, Ancaster, Canada, for whole rocks and on a VG Plasmaquad PQ1 at the Department of Geology of the Christian-Albrechts-Universität, Kiel, for feldspar separates. Analytical procedure and uncertanties have been given by Garbe-Schönberg (1993) and are available at http://www.actlabs.com.

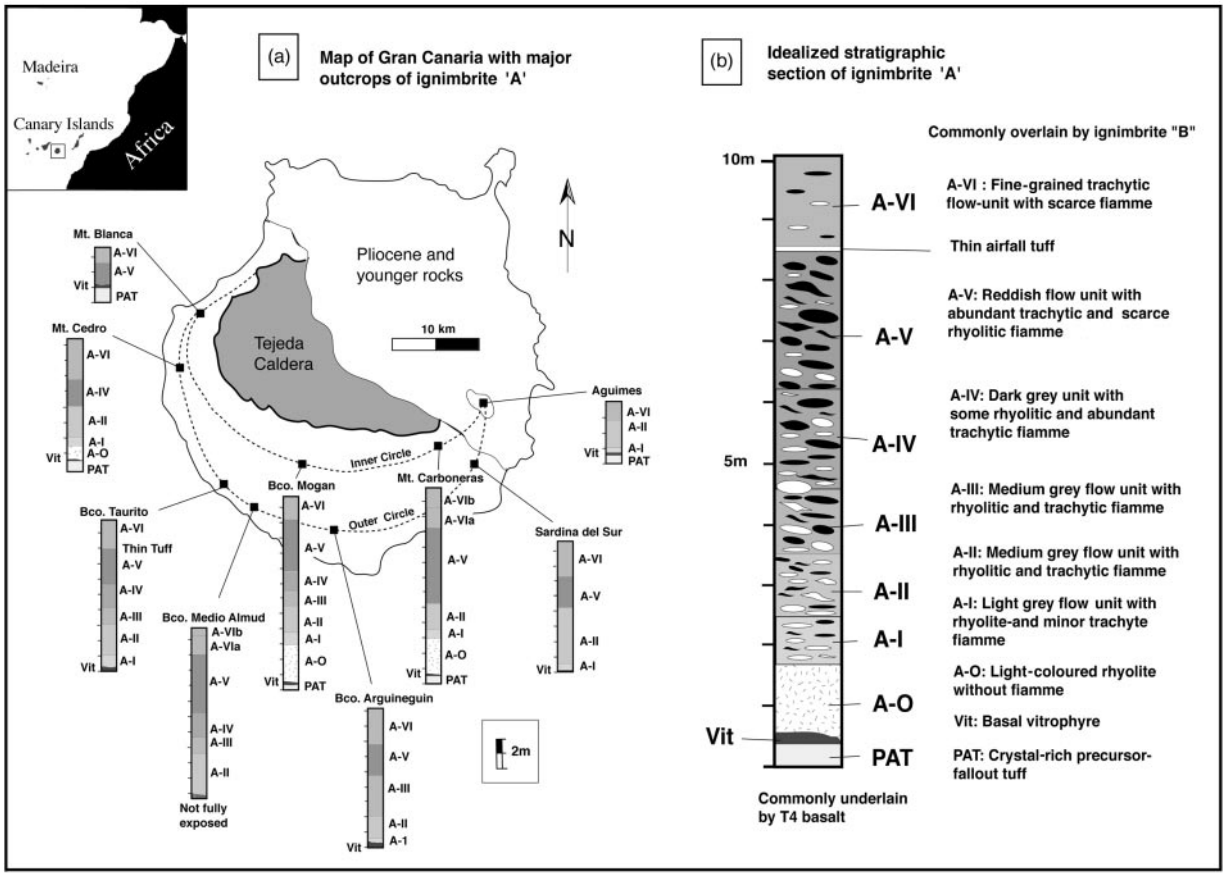

Fig. 1. Outcrop distribution and stratigraphic log section of ignimbrite 'A'.

Synchrotron-XRF

Trace element compositions in feldspar were measured with synchrotron-XRF microprobe (SYXRF) at the DORIS positron storage facility at HASYLAB/DESY-Hamburg (Troll *et al.*, 1999). Experimental setup and quantification of the spectra have been described by Lechtenberg *et al.* (1996). The primary synchrotron beam was collimated to either 50 μm × 50 μm or 30 μm × 30 μm and passed through a 100 μm thick, ultrapure Cu foil. All measurements were performed under air, and spectra were recorded with an HP Ge detector. Counting times were 1000–3600 s. Data reduction was performed using the fundamental parameter method (Janssens *et al.*, 1993; Vincze *et al.*, 1993). Detection limits are: for atomic numbers 21(Sc) to 26 (Co), 0·1–3 μg/g; for 28 (Ni) to 60 (Nd), 0·1–1 μg; for >60 (Nd), ~5 μg/g. Analytical accuracy was checked by analysis of international standards [analytical signal Kα, except Th and Pb: Lα; Hansteen *et al.* (2000), Sachs & Hansteen (2000), and are better than 5% at concentrations <100 μg/g, and better than 15% at <10 μg/g].

Oxygen isotopes

Oxygen isotopes of feldspar and whole-rock samples were analysed at the University of Cape Town by C. Harris and the University of Göttingen by J. Hoefs using a conventional vacuum extraction line employing ClF_3 (see Borthwick & Harmon, 1982; Harris *et al.*, 2000). The analytical error is estimated to be $\leq \pm 0{\cdot}15‰$. All values are given relative to standard mean ocean water (VSMOW). Feldspar separates were hand-picked under a high-magnification stereomicroscope and subsequently cleaned in a diluted HF bath for 5–10 min to remove glass and matrix from their surfaces, including removal of some material from the outer zones of the crystals as well. Whole-rock samples were also hand-picked and only carefully selected grains were used for analysis. The selected grains and crystals were free of alteration and secondary mineralization.

GEOLOGICAL SETTING

Gran Canaria, one of the central islands of the Canary archipelago, ~200 km off the NW African coast, is

underlain by Jurassic oceanic crust and pre-volcanic sediments (e.g. Rona *et al.*, 1970; Schmincke, 1976; Hoernle, 1998; Schmincke *et al.*, 1998). Gran Canaria, like the rest of the Canary Islands, belongs to an ocean island chain, thought to originate from a hotspot underneath the passive margin of the African continent (e.g. Hoernle & Schmincke, 1993).

The Miocene basaltic shield (~14–15 Ma) is overlain by ~20 peralkaline trachytic to rhyolitic (comenditic to pantelleritic) ignimbrites (Mogan Group, 13·95–13·35 Ma; Schmincke 1969, 1976; Bogaard & Schmincke, 1998), which erupted from the large (~20 km across), multiply reactivated, Tejeda caldera in the central region of the island (Schmincke, 1994; Schirnick *et al.*, 1999). The Mogan Group is overlain by a succession of some 20 phonolitic ignimbrites and lava flows (Fataga Group 13·2 to ~8 Ma) intercalated with minor basalt flows and volcaniclastic sediments. The interior of the island is thought to consist of a mafic-to-intermediate plutonic core, representing solidified parts of the Miocene shield basalts and the felsic ignimbrite succession (Freundt-Malecha, 1997; Freundt-Malecha *et al.*, 2001; Krastel & Schmincke, 2002).

The Mogan Group is subdivided into the Lower, the Mid- and the Upper Mogan Group, with subalkalic to alkalic trachyte–rhyolite ignimbrites in the Lower Mogan Group, followed by increasingly peralkaline trachyte–rhyolite ignimbrites in the Mid- to Upper Mogan Group, grading into the overlying phonolitic Fataga Group. The Mogan Group begins with the strongly zoned rhyolite–trachyte–basalt ignimbrite 'P1' interpreted to have experienced fractional crystallization and magma mixing as well as wall-rock assimilation of intermediate to felsic plutonic rocks (Freundt & Schmincke, 1995). Details on the stratigraphy, gross mineralogy and overall geochemistry of the rest of the Miocene ignimbrite succession have been given by, for example, Schmincke (1969, 1976, 1994), Crisp & Spera (1987), Cousens *et al.* (1990), Sumita & Schmincke (1998) and Freundt-Malecha *et al.* (2001).

Ignimbrite 'A' marks the onset of the transition from the Mogan to the Fataga Group (Upper Mogan Group to Lower Fataga Group), thought to be caused by the progressive input of a distinct mantle component (Cousens *et al.*, 1990). This component is best reflected in the widespread alkali-basalt flow T4 that commonly underlies ignimbrite 'A' and differs from the shield basalts' composition in being distinctly more alkaline and hence a possible candidate for the parent magma composition of the Upper Mogan and lower Fataga Groups. Ignimbrite 'A' is therefore not only an ideal candidate to study changing magmatic conditions and processes, it may also be that 'A' displays petrological and chemical features lacking in the 'pure' endmembers of the Mogan and the Fataga Group ignimbrites (compare Cousens *et al.*, 1990). So far, detailed petrogenetic studies of individual ignimbrites of the Mogan Group have been carried out only for ignimbrite 'P1' at the base of the Mogan Group (Freundt & Schmincke, 1995).

IGNIMBRITE 'A'

Stratigraphy

Ignimbrite 'A' (13·63 ± 0·3 Ma, Bogaard & Schmincke, 1998), the first unit of the Upper Mogan Group (Fig. 1), is a small-volume ignimbrite [~30 km^3 dense rock equivalent (DRE)], with a thickness of the order of 10–12 m. Ignimbrite 'A' is vertically zoned from a rhyolitic base (including proximal fallout tuffs) to a trachytic top, displaying up to seven well-defined flow units that make up the cooling unit, summarized as ignimbrite 'A' (Fig. 1). The seven flow units are thought to represent successive depositional pulses from the same magma reservoir, progressively tapping deeper levels of a compositionally layered magma chamber as envisaged by, for example, Blake (1981). Phenocryst contents generally increase upwards within 'A', as in all other ignimbrites of the Mogan and Fataga Groups. Three types of fiamme (collapsed pumice) are distinguished in outcrop: a dark grey to black trachyte, a white rhyolite and an evolved cream-coloured rhyolite.

The mineral assemblage of ignimbrite 'A'

Phenocrysts in ignimbrite 'A' rhyolites comprise anorthoclase feldspar, amphibole, Fe–Ti oxide, minor pyroxene (aegirine–augite in highly evolved pumice) and accessory phlogopite. Oligoclase to anorthoclase feldspar plus subordinate amphibole and phlogopite occur in the trachyte. The REE phase chevkinite forms rare inclusions in amphibole and/or occurs associated with oxide clusters in evolved rhyolite pumice.

Rare plastically deformed basalt schlieren occur in the trachyte-dominated flow units, showing chilled margins to the host ignimbrite and containing olivine, pyroxene and plagioclase phenocrysts. Plagioclase in the basalt occurs characteristically as skeletal groundmass crystals. The morphology of the quench crystals is typically lath-shaped with poorly defined crystal faces perpendicular to the *c*-axis, indicating undercooling of the order of 240°C or more at the interfaces of the basalt schlieren to the ignimbrite host magma (see Lofgren, 1980).

Chemical composition of ignimbrite 'A'

Ignimbrite 'A' contains three types of fiamme in a fine-grained ash matrix that is made up of shards. Angular to sub-angular lithic clasts of basalt, syenite and ignimbrite

are abundant in the ash-matrix of the lower and one of the upper flow units of the ignimbrite (locally up to 10 vol. %), comprising accidental pick-up clasts (basalt and older ignimbrite fragments) and plutonic xenoliths (mainly syenite fragments). Major element compositional trends and phase relations for the fiamme types and the whole rocks display a fairly continuous trend (Fig. 2), suggesting a differentiation sequence between two endmember compositions. The trace element spectrum of fiamme compositions, however, indicates three compositional groups or endmembers (Table 1, Fig. 3): (1) least evolved comenditic trachyte CT (SiO_2 65–67 wt %; Zr 562–615 ppm; Nb 97–112 ppm; Zr/Nb 5·79; Rb 55–68 ppm); (2) comenditic rhyolite CR (SiO_2 68–70 wt %; Zr 1127–1229 ppm; Nb 163–190 ppm; Zr/Nb 6·88; Rb 96–103 ppm); (3) evolved rhyolite RF2 (SiO_2 69–71 wt %; Zr 993–1012 ppm; Nb 99–105 ppm; Zr/Nb 10·22; Rb >113 ppm). Rhyolite RF2 differs from rhyolite CR by distinctive incompatible trace element concentrations, showing slightly higher Rb and lower Ti, Zr, Sr and Nb concentrations. Several fiamme samples appear to plot on chemical mixing lines between compositional groups, particularly between trachyte CT and rhyolite CR as well as between rhyolites CR and RF2 but not between trachyte CT and most evolved rhyolite RF2. In contrast, whole-rock data reflect physical mixing during eruption within the conduit and comprise various mixtures between the three endmember fiamme compositions. These mixing relations and the systematic vertical zonation of the ignimbrite (chiefly from early rhyolite to late trachyte) suggest a vertically zoned magma reservoir with trachyte CT at the base, progressively overlain by rhyolites CR and RF2, respectively.

FELDSPAR IN IGNIMBRITE 'A'

Abundance and petrography of feldspar phenocrysts

The major fractionating phase in all three endmembers is oligoclase to anorthoclase feldspar. Feldspar in ignimbrite 'A' is platy with abundant Karlsbad twins and with commonly broken crystals in the ash-matrix (Fig. 4a). About 70% of the feldspar phenocrysts are euhedral, the rest is made up of resorbed crystals and rare but distinct xenocrysts. The feldspar of RF2 rhyolite (~20 vol. %) are generally small (0·5–2 mm) and entirely euhedral (Fig. 4b). Rhyolite CR includes ~16 vol. % crystals up to 3 mm in size with a small population of resorbed minerals (Fig. 4c). Trachyte CT contains the largest feldspar crystals (up to 4 mm) and the highest volume of feldspar (20–30 vol. %) of which up to 45% are strongly resorbed (Table 2a; Fig. 4d). A significant percentage of the crystals in CT and, to a lesser degree, in CR and RF2 show complex internal zoning with irregular zone boundaries characterized by rounded corners and lobate embayments, and are overgrown by euhedral outer crystal zones (Fig. 4e). These textures represent overgrowth on formerly resorbed and embayed crystal faces and are classic 'partial-dissolution surfaces' in the sense of Tsuchiyama (1985).

Range of feldspar compositions

Feldspars crystallizing from each of the three endmember compositions were determined by chemical analysis of euhedral feldspar and microlite compositions in fiamme and can be distinguished from each other by their major element concentrations, in particular their Ab, Or and FeO_t concentrations (Table 2b). Trachyte CT contains feldspar with $Ab_{85–75}$ $An_{2–22}$ $Or_{13–3}$ and FeO_t ~0·4–1·3 wt %. Rhyolite CR contains feldspar with $Ab_{77–66}$ $An_{3–0}$ $Or_{20–34}$ and FeO_t ~0·6–3·0 wt %, whereas RF2 contains feldspar with $Ab_{75–65}$ $An_{5–2}$ $Or_{20–33}$ and generally low FeO_t of 0·4–0·8 wt %. Each compositional group contains only a single feldspar compositional trend with a general tendency of more evolved composition for microlites than for euhedral phenocrysts, consistent with the phase relation for single solid solutions in the system albite–orthoclase and with the ternary feldspar phase relations in the system albite–anorthoclase–orthoclase at magmatic temperatures (Nekvasil, 1994; Nekvasil *et al.*, 2000). The range in FeO_t in CR rhyolite most probably reflects the increasing degree of oxidation at lower temperatures and consequent availability of Fe_2O_3 to the crystallizing feldspars (Fe^{3+} is more compatible in alkali feldspar than Fe^{2+}), consequently raising their FeO_t content. The feldspar from endmember rhyolite RF2 shows higher anorthite but lower FeO_t contents (Figs 5 and 6), probably reflecting the onset of aegirine crystallization in RF2 type rhyolites.

A small group of mixed feldspar compositions is present (Fig. 7) suggesting the existence of transitional and/or mixed melt batches between the trachyte and rhyolite compositional groups. Ignimbrite 'A' also contains syenite nodules with feldspar compositionally and texturally similar to the phenocrystic feldspars of the rhyolite endmembers (Table 2b). Rare possible xenocrysts show compositions up to An_{50} with melt inclusions of 55–57 wt % SiO_2, suggesting them to be derived from an intermediate protolith.

Compositional zoning in feldspar

As outlined above, many feldspar crystals are compositionally zoned. Four types of zonation were distinguished from each other, including (1) normal and reverse zoning (ΔAb and ΔOr = 4 mol %), and (b) two

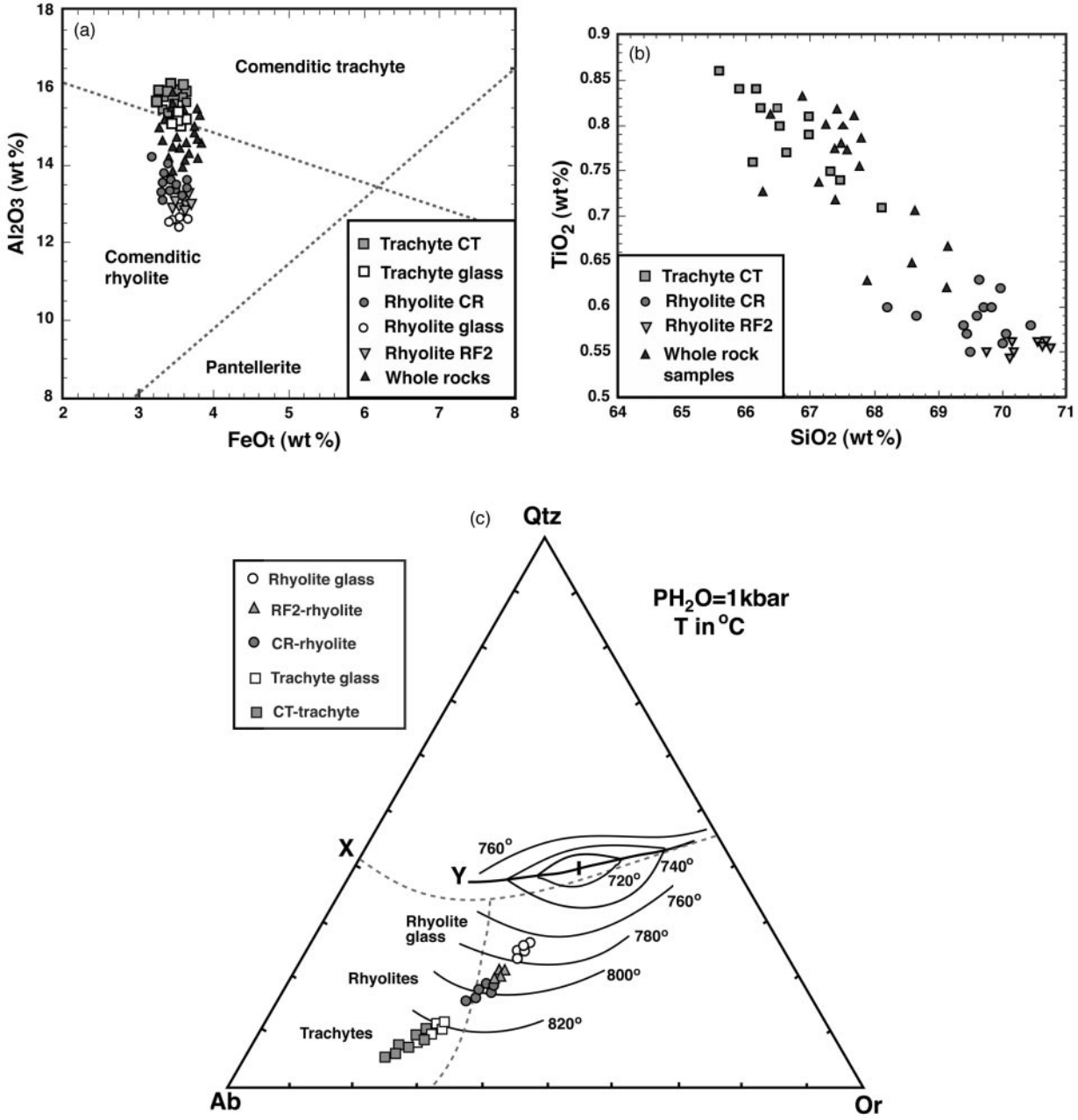

Fig. 2. (a) Classification of evolved peralkaline rocks after Macdonald (1974). The endmembers of ignimbrite 'A' can be classified as comenditic trachyte to comenditic rhyolite with variably mixed whole-rock compositions plotting between the two identifiable endmember compositions. (b) TiO_2 vs SiO_2 showing a straight TiO_2 decrease with increasing SiO_2, suggestive of a fractional crystallization sequence. (c) Qtz–Ab–Or–H_2O phase relations. Dashed line (X) represents qtz–fsp cotectic of the system $NaAlSi_3O_8$–$KAlSi_3O_8$–SiO_2–H_2O (Tuttle & Bowen, 1958). Continuous line (Y) is the qtz–fsp cotectic of the 8·3% acmite + 8·3% sodium metasilicate plane in the system $NaAlSi_3O_8$–$KAlSi_3O_8$–SiO_2–H_2O–Na_2SiO_3–$NaFeSi_2O_6$ after Carmichael & MacKenzie (1963). All samples of ignimbrite 'A' fall within the thermal valley of Carmichael & MacKenzie (1963) and evolve towards the qtz–fsp cotectic. The data follow a trend expected for fractional crystallization.

types with complex zoning (ΔAb = 14–18 mol %, ΔOr = 15–20 mol %).

Normal zoning

Normal zoning occurs throughout the compositional spectrum of the feldspars and is marked by a general decrease in Ab and increase in Or from the cores to the crystal rims in anorthoclase, and by a increase in Ab and a decrease in An in oligoclase (Figs 8a and b and 9a). Normal zoning is seen in the dominant portion of the feldspars (~45–50%) and is not associated with any internal dissolution surface; it is thus thought to reflect

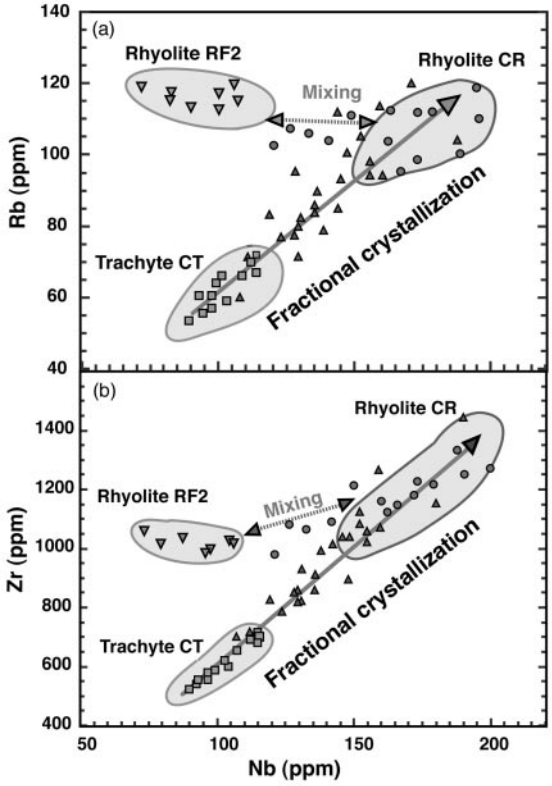

Fig. 3. Rb and Zr vs Nb (ppm) of ignimbrite 'A' fiamme and whole-rock samples. Three fiamme compositional endmembers are defined by trace element abundances, namely, trachyte CT, rhyolite CR and a second rhyolite RF2. Whole-rock samples represent variably mixed compositions between the three compositional groups.

near-equilibrium growth from a melt progressively depleted in the components crystallizing. The additional fluctuations measured are of the order of ΔAb = 3–4 mol % and are, by analogy to plagioclase, considered to lie within the compositional range of local disequilibrium and/or small pressure and temperature changes during crystal growth (Loomis, 1982; Pearce & Kolisnik, 1990). Normal zoning in ignimbrite 'A' feldspar compares with type I zoning of Pearce & Kolisnik (1990), characterized by small chemical fluctuations and not associated with a dissolution event.

Reverse zoning

Reversely zoned crystals, although less common than the normal zonation type, make up a significant percentage (25–30%) of the feldspar population. The general trend of increasing Ab towards the crystal rims in anorthoclase and the reverse in oligoclase is marked by fluctuations of the order of ΔAb = 4 mol % (Fig. 9a). This type also lacks internal dissolution surfaces and is thus considered to also fall within type I zoning of Pearce & Kolisnik (1990). However, reverse zoning requires an explanation distinct from plain fractional crystallization, as crystallization conditions in a progressively evolving chemical environment cannot satisfactorily explain a reverse zonation pattern.

Complex zoning

The two complexly zoned types comprise anorthoclase feldspar with individual zones of oligoclase composition (15–20% of feldspar population) and oligoclase with individual zones of anorthoclase composition (5–10% of feldspar population) (Fig. 9b). The observed maximum ΔAb variation ranges between 14 and 18 mol % of Ab coupled with changes of 15–20 mol % Or. Zones of different composition are generally associated with one or more major internal dissolution surfaces (Figs 4e, 8c and 9b). The zones range in width from a few microns to several hundred microns and fall clearly within the oligoclase field in the case of an anorthoclase core and rim, and in the anorthoclase field in the case of an oligoclase core and rim (Fig. 8c). The latter type is less common and often shows dissolution surfaces that are less pronounced. A significant percentage of crystals is characterized by a core of either oligoclase or anorthoclase that is mantled by anorthoclase or oligoclase, respectively, without, however, a shift back to their core composition in the outer zones of the crystals.

The drastic changes among zones of the two complexly zoned types are not restricted to Ab, An and Or content but are also reflected in the FeO_t. A representative rim-to-rim profile (Fig. 10) shows two extreme anorthite minima extending downwards from a plateau of uniform oligoclase feldspar to anorthoclase feldspar compositions. Subsequent zones from the core outwards show again a fairly homogeneous oligoclase composition. This trend is reversed for the FeO_t content of the feldspar zones.

Neither convection within a single fluid or melt body nor gentle pressure and temperature changes appear able to produce such drastic compositional changes of up to 18 mol % Ab and 2·5 wt % FeO_t, and a more elaborate model is required to explain this type of zonation. Taking Ab and Or instead of An as the sensitive parameters (because of the low An content), these types compare well with the type II zoning pattern of Pearce & Kolisnik (1990) and Pearce (1994), which is marked by zones of drastically different compositions, commonly associated with one or more major dissolution surfaces. This type of zoning is thought to clearly indicate the changing chemical environments a crystal was subjected to.

A subtype of complex zonation occurs exclusively in rhyolite feldspar. This type is marked by zones characteristic of one of the endmember rhyolites with zones of another rhyolite feldspar characteristic of the other endmember rhyolite. Figure 11 shows a zoning pattern for a rhyolitic feldspar with two minima also of rhyolite

Table 1: Representative whole-rock and fiamme XRF analyses

	Whole rocks												
Sample no.:	T4-Basalt	A-O-MCa	AI-MCa	AII-Agu	AII-MC	AIII-BTTS	AIII-Bto	AIV-BTO	AIV-Bto-TS	AV-BTTS	AVa-BTo	AVIb-BTTS	AVI-BTo
SiO_2	43·69	69·22	69·27	67·03	67·5	67·83	68·7	67·4	67·35	67·52	67·17	67·55	67·16
TiO_2	4·62	0·63	0·68	1·17	0·78	0·75	0·71	0·82	0·71	0·8	0·85	0·77	0·74
Al_2O_3	15·06	14·15	14·47	13·66	14·75	15·35	14·57	15·31	14·89	15·66	15·19	15·61	15·09
Fe_2O_3	14·07	3·62	3·56	5·21	3·86	3·47	3·64	3·76	3·34	3·49	3·83	3·46	3·4
MnO	0·19	0·15	0·15	0·23	0·14	0·11	0·18	0·13	0·13	0·13	0·17	0·12	0·14
MgO	5·86	0·3	0·29	0·83	0·36	0·28	0·28	0·43	0·47	0·33	0·56	0·34	0·5
CaO	11·22	0·22	0·36	1·15	0·56	0·34	0·58	0·53	0·48	0·64	0·5	0·37	0·72
Na_2O	2·96	6·25	6·58	6·37	6·42	7	6·76	6·94	7·26	7·15	6·82	6·96	7·11
K_2O	1·28	4·8	4·39	4·12	4·36	4·12	4·41	4·08	4·17	3·66	4·02	4·17	4·03
P_2O_5	0·76	0·04	0·06	0·14	0·06	0·07	0·09	0·07	0·1	0·12	0·09	0·05	0·07
Total	99·71	99·38	99·81	99·91	98·79	99·32	99·92	99·47	98·9	99·5	99·2	99·4	98·96
Ba	308	242	693	537	686	1419	635	1031	935	1575	1224	1047	1108
Co	41	<4	<4	6	5	5	4	5	5	5	6	5	5
Ce	184	375>	397>	395>	377>	300>	364>	274>	328>	315>	263>	201	336>
La	<14	87	93	72	113	90	81	87	104	80	67	64	101
Nb	57	153	148	138	155	131	146	135	119	112	130	150	123
Ga	19	35	36	36	32	32	34	35	31	28	31	33	35
Pb	<4	9	7	<4	6	9	5	8	6	9	9	<4	7
Rb	31	115	100	79	98	82	94	83	83	71	80	77	76
Sr	1007	24	30	78	60	52	46	67	45	69	75	36	46
Th	<4	16	19	11	16	17	21	19	13	7	15	7	12
V	445	27	31	64	36	27	35	30	28	23	29	28	21
Y	31	63	69	61	71	53	66	57	54	53	55	52	59
Zr	424	1080	1037	992	1029	825	1037	855	834	711	855	885	783
Zn	123	165	159	185	160	122	150	141	120	123	151	139	130

	CT-type fiamme				CR-type fiamme					RF2-type fiamme			
Sample no.:	AIII- F38	A III-F3-BTo	AIII-F8-BTo	AIV-F6-Bto	AV-F32-Bto	AV-F27-Bto	AIII-F28-Bto	AIII-F12-Bto	AII-F9-Mca	AIV-F2-BTTS	AIII-F11-Bto	A-F40-Bto	A-F20-Btau
SiO_2	65·89	66·1	67·59	66·98	68·65	69·71	69·44	69·39	69·96	70·51	70·63	70·7	70·67
TiO_2	0·84	0·76	0·73	0·79	0·59	0·6	0·57	0·58	0·62	0·56	0·56	0·56	0·56
Al_2O_3	16·02	15·57	15·35	16·02	13·52	13·8	13·73	14·3	13·8	13·27	13·25	13·27	13·27
Fe_2O_3	3·36	3·25	3·2	3·25	3·35	3·45	3·36	3·24	3·63	3·61	3·63	3·59	3·61
MnO	0·12	0·12	0·14	0·13	0·15	0·17	0·18	0·19	0·17	0·16	0·16	0·16	0·16
MgO	0·47	0·45	0·41	0·45	0·11	0·14	0·15	0·29	0·13	0·09	0·19	0·19	0·18
CaO	1·11	0·84	0·68	0·85	0·25	0·27	0·28	0·3	0·21	0·24	0·25	0·25	0·24
Na_2O	7·67	7·67	7·41	7·63	7·39	6·72	6·45	6·49	6·34	6·26	6·29	6·26	6·27
K_2O	3·15	3·7	3·79	3·37	4·34	4·54	4·69	4·65	4·71	4·81	4·83	4·83	4·83
P_2O_5	0·16	0·14	0·1	0·15	0·04	0·05	0·05	0·05	0·04	0·04	0·04	0·04	0·04
Total	98·79	98·6	99·4	99·62	98·39	99·45	98·9	99·48	99·61	99·55	99·83	99·87	99·83
Ba	2351	1574	1512	2130	243	287	209	319	338	117	118	120	149
Co	7	6	5	6	4	<4	<4	<4	<4	<4	<4	<4	<4
Ce	292>	324>	293>	327>	455>	463>	346>	385>	317>	248	279>	271>	290>
La	86	85	59	81	135	128	112	107	74	63	55	56	61
Nb	93	103	112	97	171	163	142	118	161	104	105	56	61
Ga	30	32	33	37	36	34	38	35	33	35	35	35	34
Pb	8	10	6	9	11	10	11	11	6	9	10	6	8
Rb	60	59	70	57	96	103	103	93	113	119	115	116	119
Sr	48	13	24	22	16	16	5	5	15	7	10	10·78	9·89
Th	11	12	13	8	23	20	23	15	19	25	24	14	20
V	29	31	28	29	19	14	20	24	32	34	37	34	30
Y	48	57	51	49	76	71	50	55	63	54	55	54	55
Zr	560	598	692	562	1178	1127	1090	909	1159	1019	1012	1019	1017
Zn	120	106	122	111	112	124	141	124	186	140	144	140	142

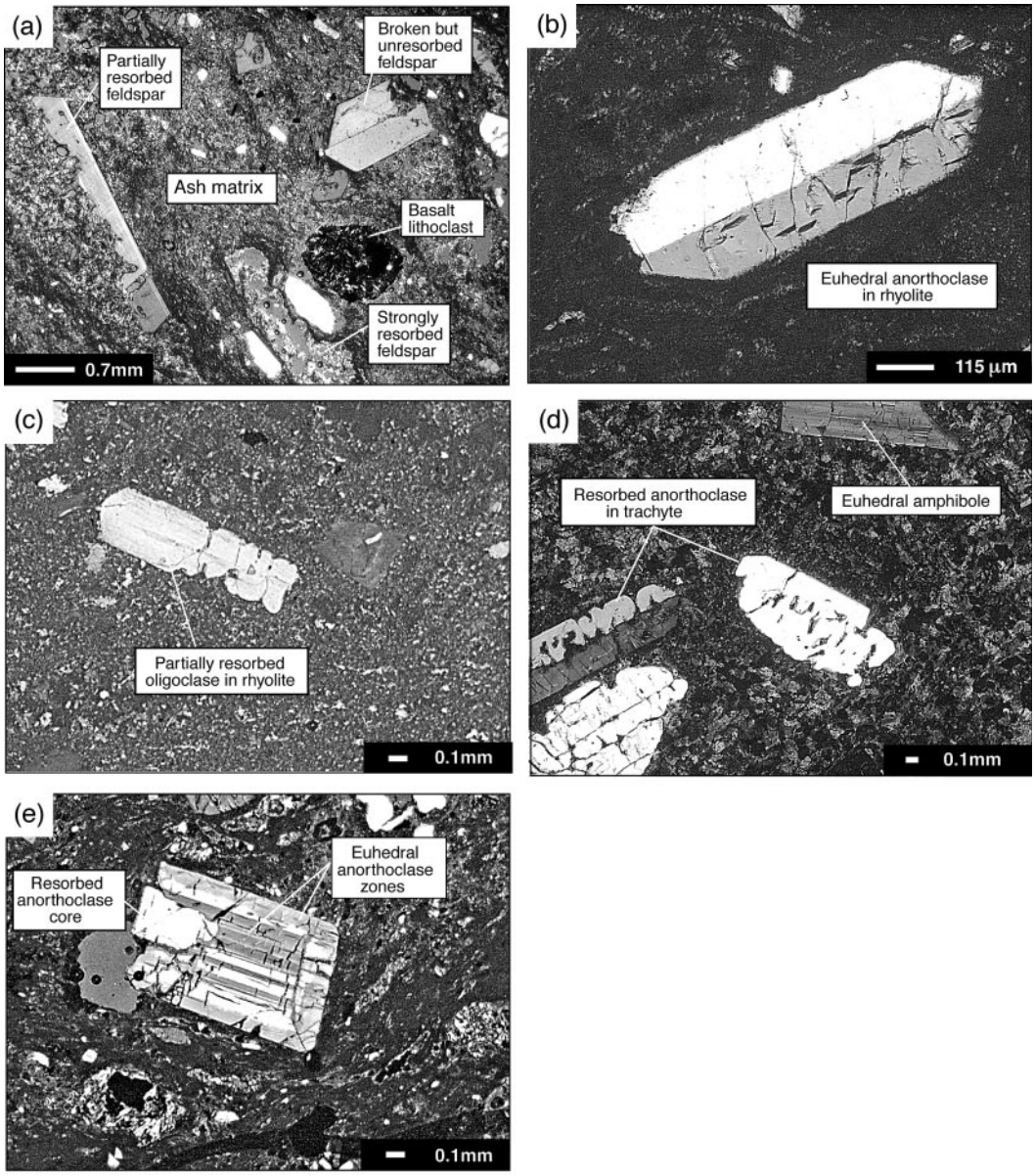

Fig. 4. Photomicrograph of feldspar textures (all under cross-polarized light). (a) Tuff matrix of mixed unit IV, showing broken but euhedral crystals together with variably resorbed crystals and lithic fragments. (b) Euhedral anorthoclase crystal in rhyolite fiamme. (c) Partially resorbed oligoclase crystsl in rhyolite fiamme. (d) Strongly resorbed anorthoclase crystals in trachyte fiamme. (Note euhedral amphibole top centre.) (e) Crystal fragment in tuff matrix of flow unit V with complex internal zoning. An anhedral anorthoclase core is mantled by two major euhedral anorthoclase growth zones.

feldspar composition (ΔAb 6%). The two minima, however, show an FeO_t content of >2·5 wt % characteristic for the Fe^{3+}-rich CR type feldspar. The feldspar composition of the other zones is fairly homogeneous but with an FeO_t content of 0·5–0·8 wt % and therefore representative of the less oxidized CR feldspar and/or the RF2 endmember feldspar.

Trace and rare earth elements

Trace elements

A small (<1 mm) euhedral and normally zoned feldspar crystal was selected from CR and RF2 rhyolites to evaluate the trace element composition of the feldspars that formed late in the two rhyolites. A euhedral normally

Table 2a: Feldspar abundance and proportions

Sample no.	Compositional group	fsp modal %	Max. size (mm)	Euhedral fsp (%)	Resorbed fsp (%)
A-III-F37-BTo	CT trachyte	26	4	60	40
A-III-F8-BTo	CT trachyte	20	3	55	45
A-IV-F6-Bto	CT trachyte	22	3·5	60	40
A-III-F34-BTo	CR rhyolite	14	2	80	20
A-II-F27-MBTo	CR rhyolite	12	1·5	85	15
A-II-F21-MCa	CR rhyolite	12	1·5	90	10
A-F2-BTTo	RF2 rhyolite	18	0·5	100	0
A-II-F31-BTo	RF2 rhyolite	15	1·5	100	0
A-F11-BTo	RF2 rhyolite	16	1	100	0

zoned crystal of ~2 mm size was also selected from CR rhyolite, thought to represent a feldspar that grew 'early' in CR. The two small crystals are both Or-rich anorthoclase, whereas the larger crystal from CR rhyolite is an Or-poor anorthoclase. Major and trace element concentrations were determined by EMP and SYXRF analysis (Table 3, Fig. 12). Analyses were performed within the same zone of each crystal to guarantee the feldspar type and the accuracy of the SYXRF analyses.

A slight enrichment in Nb, Sr, Zr and Rb coupled with a slight depletion in Ba appears to be characteristic for the Or-rich CR feldspar relative to the Or-poor CR feldspar. In contrast, the feldspar from rhyolite RF2 shows a drastic depletion in Sr, Nb and Zr relative to both CR feldspars. Elements such as Ti and Y are, in turn, slightly enriched in RF2 feldspar relative to CR feldspars. Pb and K are virtually identical for all three feldspars.

Rare earth elements

Rare earth elements were determined by ICP-MS for several whole-rock fiamme compositions and feldspar separates from the three compositional fiamme groups, the latter including the lowermost ignimbrite 'A' fallout tuff (PAT samples).

The fiamme data show the endmember compositions of rhyolite CR and trachyte CT to run approximately parallel (Table 4; Fig. 13a and b). The trachytes are generally less enriched in REE than CR rhyolites, except for Eu, for which the trachytes display a positive anomaly. The CR and RF2 rhyolites show only a minor to absent Eu trough. RF2 fiamme do, however, not run parallel to the CT and CR patterns and are depleted in LREE and middle REE (MREE), but crosscut the trachyte pattern at Tb and Gd, followed by an enrichment of heavy REE (HREE) relative to CT. The RF2 rhyolites also lack the significant Eu trough expected for substantial feldspar removal. We also show a reference pattern taken from Freundt & Schmincke (1995) for an uncontaminated 'P1' rhyolite whole rock, showing a well-defined negative Eu anomaly as expected for rhyolites that precipitated large quantities of feldspar subsequently removed by crystal fractionation (Fig. 13).

Feldspar separates of all three compositional groups show a distinct positive Eu anomaly with similar Eu concentrations in all three groups. LREE concentrations, on the other hand, are lowest in trachyte-derived feldspar separates and show significantly higher abundances in rhyolite-derived feldspar separates, with little difference between CR and RF2 feldspars. For HREE, trachyte feldspar separates again contain the lowest concentrations, whereas CR and RF2 feldspars are enriched in HREE, with RF2 feldspar showing the highest concentration of HREE.

RF2 fiamme are thus marked by a depletion in incompatible trace elements and LREE relative to CR, although showing a slight enrichment in compatible elements and HREE relative to CT. Depletion of incompatible elements in RF2 fiamme is consistent with the *in situ* feldspar data, where RF2 feldspar is characterized by lower concentration of incompatible elements relative to CR feldspars, but contains higher concentrations of Ti and Y. Feldspar separates that represent a spectrum of 'early to late' crystals reflect this LREE depletion less clearly but show significantly higher concentrations of HREE in RF2 feldspar, consistent with higher Ti and Y in *in situ* feldspar data.

OXYGEN ISOTOPES

Oxygen isotopes of feldspar separates vary among the endmember types, displaying an overall range of $\delta^{18}O =$

Table 2b: Representative feldspar analyses for the four zoning types and xenocyst feldspar of ignimbrite 'A'

	Fsp 31-type I			Fsp 7b-type I			Fsp22-type II			Fsp 29-type II		
Position:	Core-Ry	Spot 12-Ry	Rim-Ry	Core-Tr	Spot 10-Tr	Rim-Tr	Core-Ry	Spot 11-Ry	Rim-Ry	Core-Tr	Spot 10-Tr	Rim-Tr
Spot no.:	S2-226	S2-238	S2-250	S1-177	S1-183	S1-190	S2-75	S2-64	S2-56	S2-181	S2-191	S2-200
SiO_2	66·85	66·56	67·119	65·04	65·31	65·87	67·43	66·15	66·08	64·73	64·49	64·31
Al_2O_3	18·89	18·74	18·797	21·36	21·14	20·8	18·88	18·87	18·87	21·33	21·18	21·41
CaO	0·16	0·08	0·102	2·06	1·93	1·45	0·11	0·29	0·24	2·08	2·33	2·3
FeO_t	0·65	0·83	0·858	0·48	0·48	0·51	0·74	0·58	0·59	0·41	0·52	0·55
BaO	0·24	0·14	0·04	0·71	0·8	0·79	0·15	0·33	0·28	0·79	0·79	0·67
Na_2O	8·55	8·41	8·17	9·27	9·38	9·6	8·19	8·72	8·69	9·41	9·38	9·23
K_2O	4·46	4·64	4·745	1·35	1·32	1·41	4·44	4·07	3·8	1·12	1·08	1·31
Total	99·81	99·4	99·83	100·27	100·36	100·43	99·93	99·01	98·55	99·87	99·77	99·78
Ab mol%	73·55	72·92	71·94	81	81·71	83·54	73·13	75·05	76·38	82·12	81·33	80·34
An mol%	0·76	0·52	0·5	9·95	9·29	6·89	0·54	1·35	1·16	10·04	11·12	11·04
Or mol%	25·26	26·04	27·49	7·74	7·58	8·1	26·06	23·03	21·97	6·43	6·16	7·45
Cs mol%	0·43	0·24	0·07	1·25	1·42	1·39	0·27	0·57	0·49	1·4	1·38	1·17

	Fsp 5-type III					Fsp 6-type IV					Xeno-Fsp in CR	Syenite-Fsp in plutonite
Position:	Core-Tr	RZ 1	TZ	RZ2	Rim-Tr	Core-Tr	RZ	TZ1	TZ2	Rim-Ry		
Spot no.:	S1-105	S1-112	S1-117	S1-121	S1-130	S1-161	S1-156	S1-148	S1-139	S1-135	A-V-EMC-5	A-V-Bto-8
SiO_2	65·91	66·68	65·94	67·12	65·59	66·35	66·36	65·42	64·68	71·55	54·65	67·13
Al_2O_3	20·78	16·22	20·81	15·88	19·76	19·35	18·88	19·81	20·36	14·13	27·62	19·96
CaO	1·37	0·62	1·43	0·63	1·37	0·86	0·12	0·69	1·21	0·11	10·48	0·59
FeO_t	0·44	2·8	0·54	2·64	0·59	1·21	0·69	0·53	0·45	2·24	0·72	0·52
BaO	0·52	0·33	0·65	0·27	0·68	0·67	0·11	0·65	0·77	0·12	0·06	0·09
Na_2O	9·39	7·07	9·3	7·39	9·36	9·13	8·47	9·57	9·53	6·75	5·45	6·74
K_2O	1·73	5·06	1·72	4·46	2·11	2·42	4·67	2·06	1·83	3·84	0·33	4·41
Total	100·14	98·78	100·39	98·39	99·46	99·99	99·3	98·73	98·83	98·74	99·31	99·44
Ab mol%	82·36	65·44	81·88	68·9	81·99	80·57	72·88	83·71	82·5	72·14	47·5	67·54
An mol%	6·67	3·15	6·97	3·23	6·87	4·22	1·25	3·29	6·1	2·86	50·5	3·24
Or mol%	10·03	30·79	9·96	27·38	9·88	14·02	26·41	11·85	9·79	27·01	1·9	29
Cs mol%	0·94	0·61	1·19	0·49	1·26	1·2	0·2	1·15	1·16	0·09	0·11	0·19

Ry, rhyolitic anorthoclase; Tr, trachytic oligoclase; RZ, rhyolitic anorthoclase zone; TZ, trachytic oligoclase zone. Feldspar- and spot numbers refer to Fig. 9a and b.

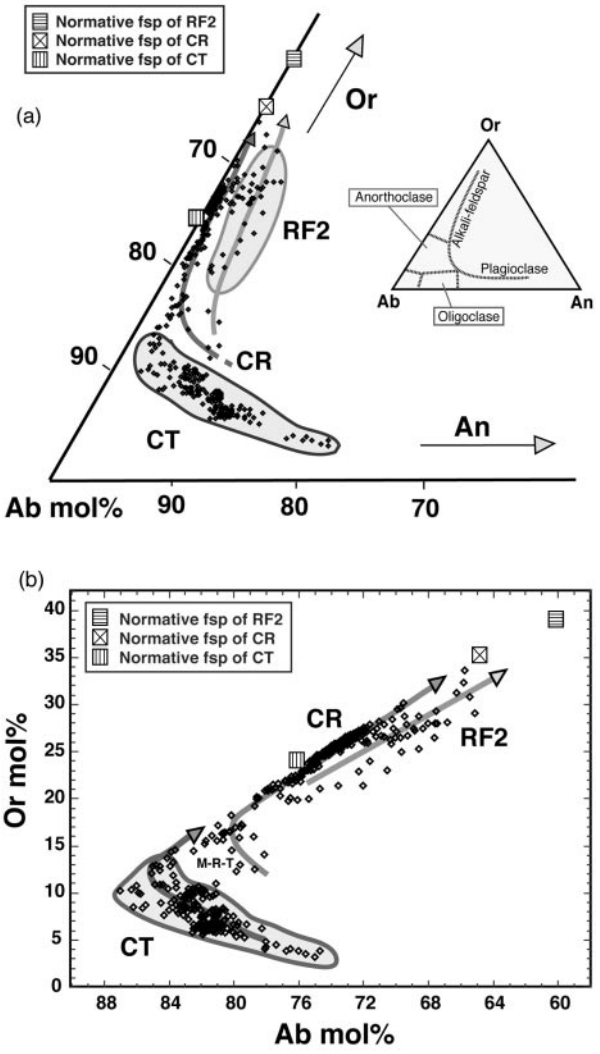

Fig. 5. (a) Lower left corner of Or–Ab–An triangle showing the compositional fields of feldspar in ignimbrite 'A'. Squares represent the normative feldspar of the corresponding endmember magma types. (b) Ab mol % vs Or mol % of ignimbrite 'A' feldspar defines three groups with distinct compositions corresponding to the three magmatic endmembers. The mixed feldspar compositions between the CR and CT groups (M–R–T) should be noted.

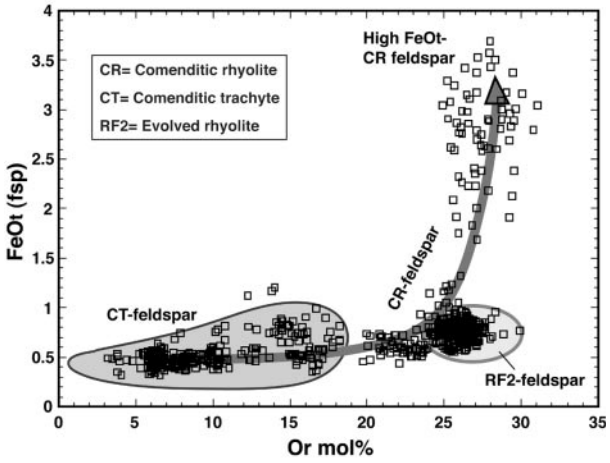

Fig. 6. FeO_t (fsp) vs Or mol % of ignimbrite 'A' feldspar illustrates the low FeO_t content of CT and the increasing FeO_t content of CR feldspar towards higher Or content. RF2 feldspar plots in a narrow field at low FeO_t and high Or mol %.

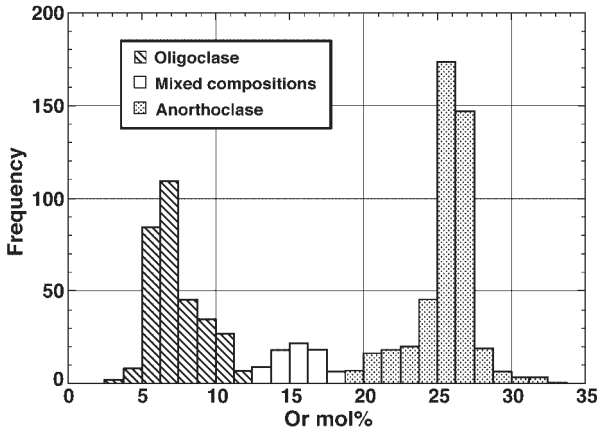

Fig. 7. Feldspar compositions (Or mol %) representing ~1000 EMP spot analyses. The frequency plot suggests a higher abundance of rhyolite feldspar within ignimbrite 'A' relative to trachyte feldspar with a small intermediate group of mixed feldspar compositions.

6·4–7·32‰ (±0·15‰), characteristic values for a highly evolved, silica-saturated rock suite (Table 5, Fig. 14). The CR rhyolite feldspar samples lie generally between 6·4 and 6·8‰, whereas RF2 samples show a narrow range of 7·1–7·32‰. One feldspar sample of the CR type also shows an elevated value of 7·20‰. Trachyte feldspar separates lie between 6·68 and 7·23‰, reflecting many feldspar crystals in the trachyte to be actually rhyolite-derived anorthoclase (consistent with the strongly resorbed anorthoclase feldspar crystals in thin section of trachyte). For one CR type rhyolite feldspar separate, sample A-F32-Bto ($\delta^{18}O_{fsp}$ of 6·68‰), a corresponding whole-rock analysis yielded $\delta^{18}O_{whole\ rock}$ of 7·83‰. This strongly suggests an oxygen isotope disequilibrium between the feldspars and their melt ('melt only' calculates to a value of ~8·1‰). This result is broadly consistent with analysis of two rhyolite glass shards with secondary ionization mass spectrometry (SIMS), analysed by A. Gurenko in Nancy [see Gurenko *et al.* (2002) for analytical details and setup], yielding 7·8 and 8·6 (±0·5‰).

Major post-depositional alteration as a process modifying the $\delta^{18}O$ of the feldspar crystals is ruled out. If such modifications had been the cause for the $\delta^{18}O$ variations, a more random set of values would be expected, especially as all samples are from different localities. The whole-rock and glass values, on the other hand, may be more suspect, as the ignimbrite matrix

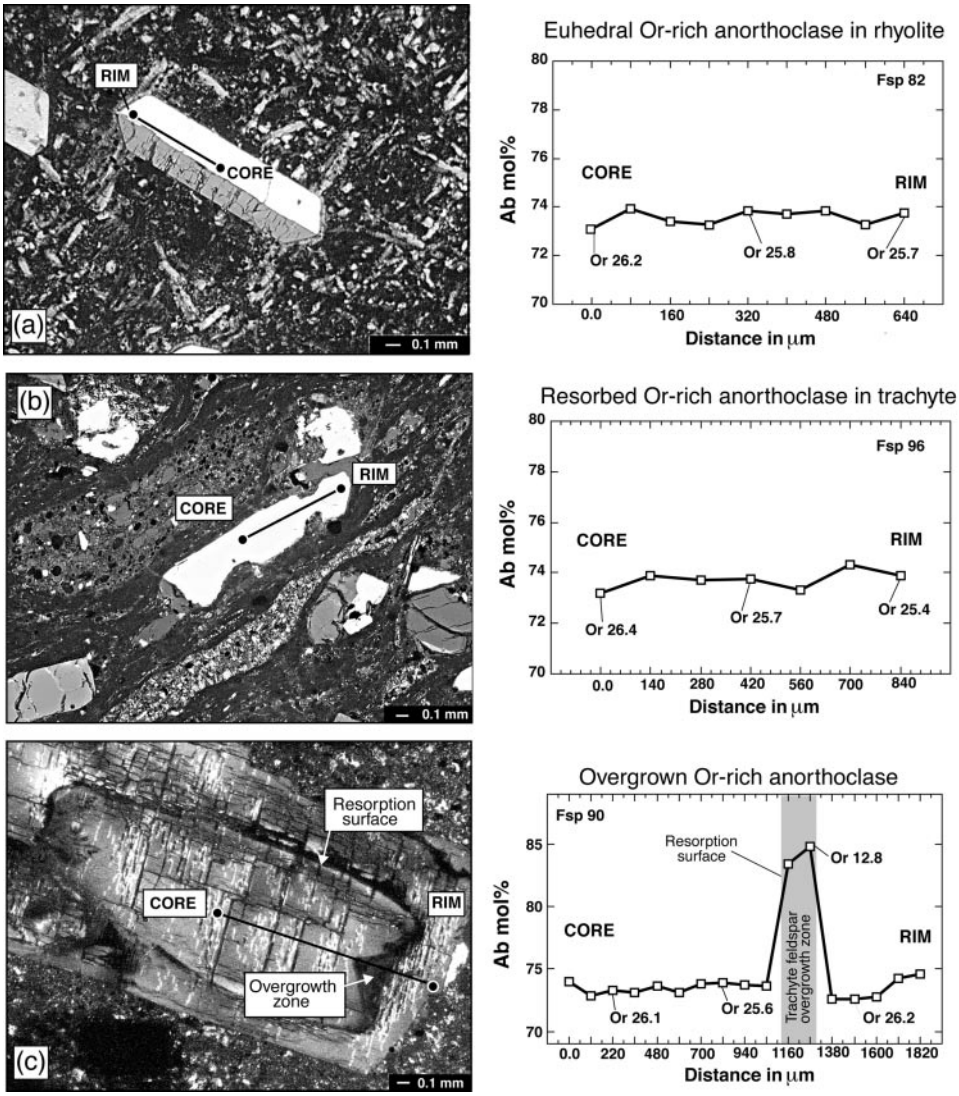

Fig. 8. Photomicrographs of feldspar (all cross-polarized light) and compositional traverses. (a) Euhedral Or-rich anorthoclase in rhyolite with homogeneous chemical composition. (b) Resorbed Or-rich anorthoclase in trachyte and (c) complexly zoned feldspar crystal with Or-rich core marked by a dissolution surface and mantled by a rind of oligoclase, which, in turn, is overgrown by a euhedral zone of Or-rich feldspar.

may have exchanged oxygen with percolating surface and/or ground water. However, no evidence for post-depositional fluid–rock interaction was found in thin section of these samples, nor did the whole-rock sample yield any anomalous H_2O and LOI values in bulk analysis. We infer the 7·83‰ whole-rock value, and in combination with the SIMS data on the glass shards an average of ~8·1‰ for the rhyolite glass, to represent real magmatic values. The resulting $\Delta^{18}O_{melt\text{-}fsp}$ is thus of the order of 1·4, well beyond the rate of $\Delta^{18}O_{melt\text{-}fsp}$ of 0·1–0·5‰ predicted for closed-system fractionation in rhyolites (Taylor & Sheppard, 1986).

PHYSICAL CONDITIONS

Temperature (*T*)

Crystallization temperatures were estimated using several independent mineral thermometers. The crystallization temperature of a silicate melt can be estimated using the partition coefficient between K/Na in amphibole (A-site) and the K/Na of the melt, represented by fresh glass measured with EMP (electron microprobe) (Helz, 1979). The crystals selected were all included in fiamme and euhedral, and we infer them to have been in textural equilibrium with the host magma (see Appendix for

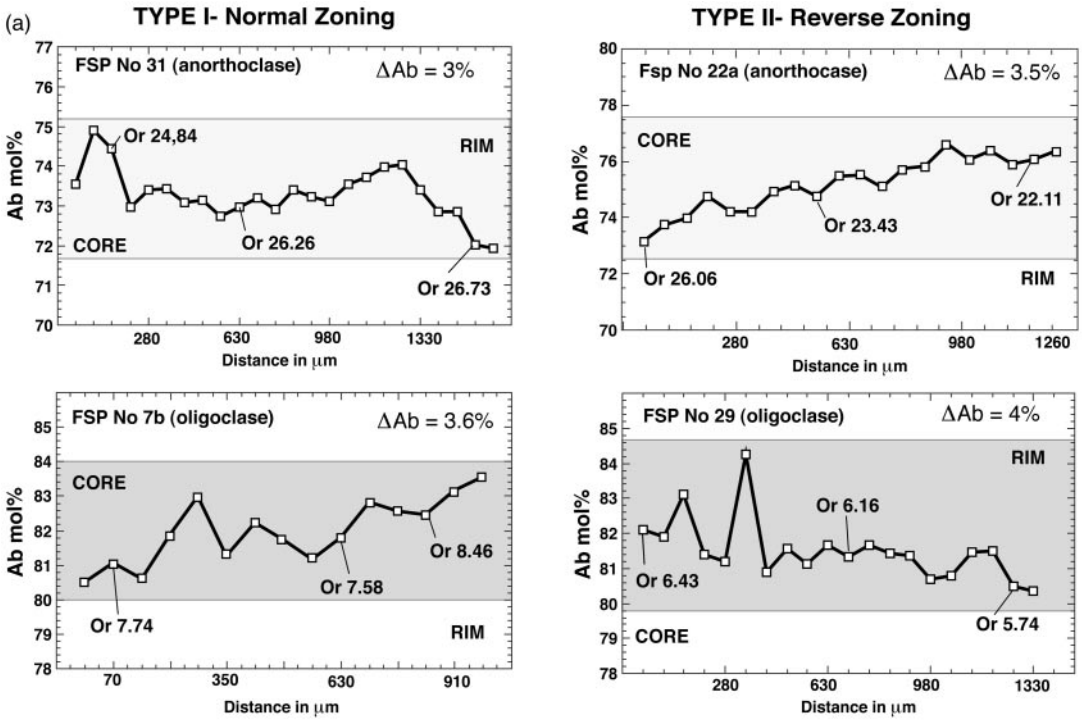

Fig. 9a.

representative analysis of amphiboles, matrix glass and melt inclusions). The temperatures calculated for ignimbrite 'A' range from 760 to 830°C ± 30°C for rhyolitic to trachytic compositions, respectively, with a gradual overlap of temperatures for the two compositions. Minimum homogenization temperatures were calculated from major element compositions of primary melt inclusion and are of the order of 755 ± 40°C for the rhyolite inclusions and 795 ± 40°C for the trachyte inclusions, using the empirical equation of Thomas (1990). The results compare well with the phase relations for the system Qtz–Ab–Or, where the trachytes plot above the 820°C isotherm and the rhyolite samples crosscut the 800°C isotherm, almost reaching the 780°C isotherm for the most evolved samples. Rhyolite glass, in turn, plots between the 760°C and the 780°C isotherms (Fig. 4c). The results are consistent with the temperature estimate of 838°C by Crisp & Spera (1987).

Pressure (*P*)

Pressure estimates based on Al-in-amphibole (see Johnson & Rutherford, 1989; Anderson & Smith, 1995) cluster around an amphibole crystallization pressure of 1·3–1·6 ± 0·5 kbar for euhedral rhyolite-derived amphiboles and between 1·9 and 2·2 ± 0·5 kbar for trachyte-derived amphiboles, although with a broad overlap within the error limit of the method. This translates to a depth of 5–7 km beneath the Miocene land surface. The shallow nature of the magma chamber is also indicated by low Al-pyroxene in the rhyolite, which contains virtually no Al^{IV} at a total Al content of the order of 0·3 wt %, consistent with Al^{IV} not being accommodated in pyroxene at low pressures (Grove *et al.*, 1989). Crisp & Spera (1987) also suggested a shallow-level magma chamber with a total pressure of 2·7 ± 3 kbar for ignimbrite 'A' (based on Fe–Ti–oxide–silica equilibrium reactions) but noted that their estimate is not well constrained.

H_2O content

The H_2O contents of the magma compositional groups were estimated by analysis of primary melt inclusions (i.e. trapped during progressive crystal growth) in euhedral anorthoclase feldspar enclosed in rhyolite fiamme and in euhedral oligoclase feldspar enclosed in trachyte fiamme. The rhyolite inclusions contain 3·0–4·0 wt % H_2O, whereas the trachyte inclusions have lower H_2O contents between 1·5 and 3·0 wt %, determined by the difference method, which is associated with an error of approximately ±0·5 wt % (Devine *et al.*, 1995) (see Appendix for representative analyses). Considering that melt inclusions preserve a former stage of the magmatic evolution, syn-eruptive H_2O contents may have been slightly higher than recorded in the melt inclusion data. By analogy, in calc-alkaline suites the crystallization overlap

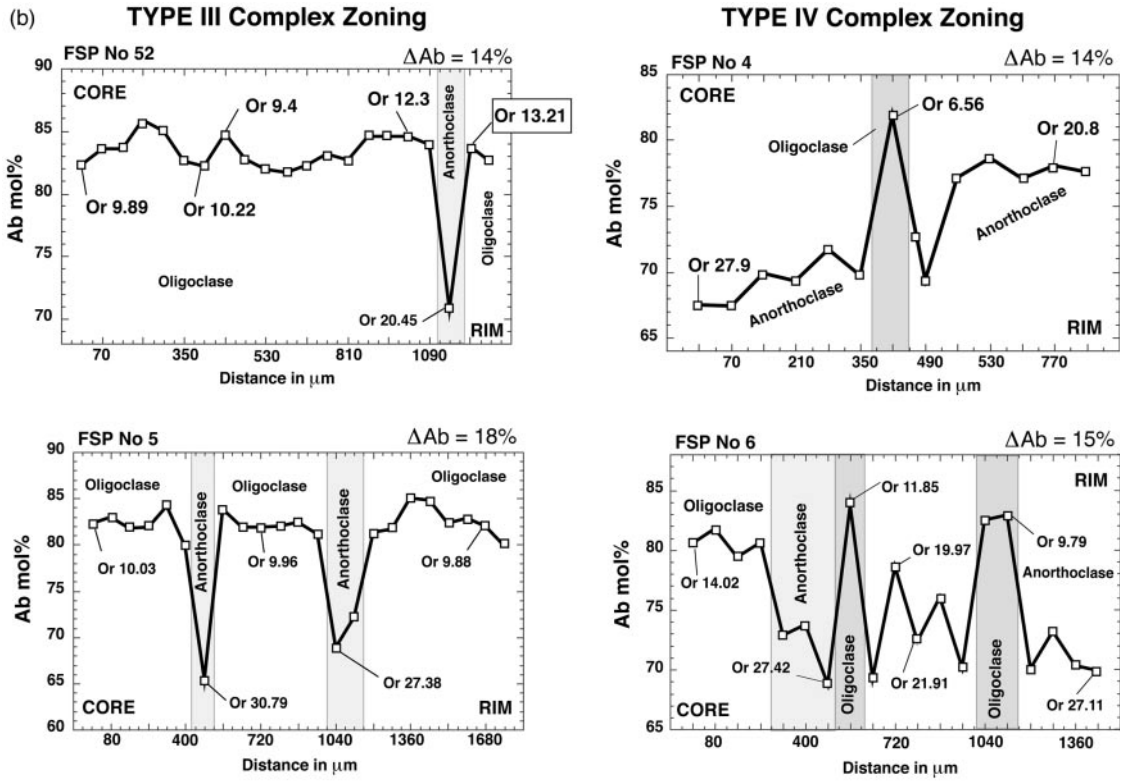

Fig. 9. (a) Compositional zonation profiles (core–rim) for several representative normal (type I) and reversely (type II) zoned feldspar crystals. The Ab mol % contents show only minor fluctuations between measurement points and overall changes of at most 4–5 mol % Ab. (b) Compositional zonation profiles for several representative complexly zoned feldspar crystals. The difference in Ab scale relative to that in (a) should be noted. Shaded vertical bars represent zones associated with a petrographically distinct dissolution surface. Type III zonation is characterized by fairly homogeneous core compositions followed by sharp drops in Ab content, which, in turn, are followed by zones similar to the core composition. Such sharp drops may occur repeatedly within the same crystal. Type IV zonation contrasts with type III zonation by sharp increases in Ab mol % often followed by markedly different compositional zones not necessarily equivalent to the core compositions (i.e. intermediate compositions).

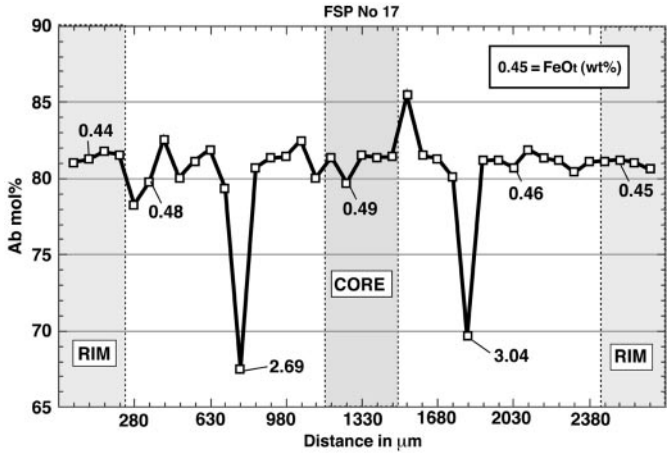

Fig. 10. Representative profile (rim to rim) of type III feldspar showing two symmetric Ab-depleted zones on either side of the crystal core followed by zones with a composition similar to the core. Small numbers represent the FeO_t (wt %) composition of individual measurement points. The high FeO_t content of the low Ab zones compared with the FeO_t content of the Ab 80–85 mol % zones should be noted.

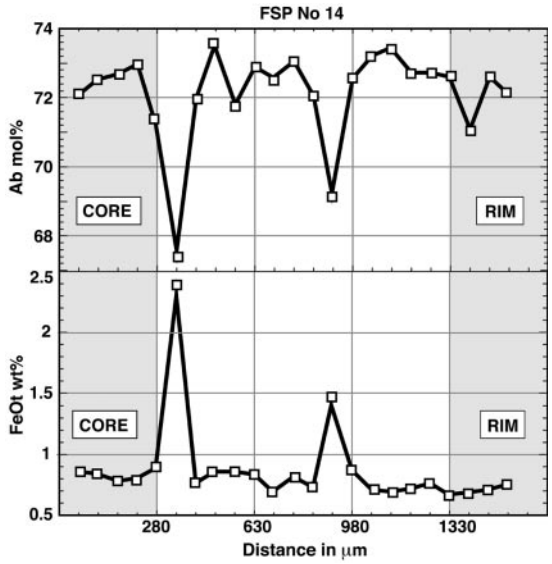

Fig. 11. Core–rim profile through a rhyolite feldspar showing two Ab-depleted but FeO_t-enriched zones, each succeeded by zones of low FeO_t and higher Ab.

of anorthoclase and amphibole (as seen in rhyolite of ignimbrite 'A') is thought to occur under low pressures and H_2O contents ≥ 4 wt % (Naney, 1983), consistent with the phase assemblage in ignimbrite 'A' rhyolites. The H_2O contents determined suggest that ignimbrite 'A' magmas were H_2O undersaturated at the given pressure and would have reached H_2O saturation at a total pressure of 1 kbar for the rhyolite and 500–1000 bar for the trachyte, relative to the experimental H_2O rhyolite solubility curve of Silver *et al.* (1990).

Crisp & Spera (1987) calculated the H_2O content for various Mogan ignimbrites and suggested a range of 0·9–2·5 wt % H_2O for most ignimbrites including ignimbrite 'A'. Their H_2O content overlaps with that found in the trachyte melt inclusions of this study. Water contents of >4 wt % were demonstrated for some rhyolite compositions of ignimbrite 'P1', the lowest ignimbrite of the Mogan Group (Freundt & Schmincke, 1995).

Oxygen fugacity (fO_2)

Ignimbrite 'A' contains only a single oxide in the rhyolite endmembers—a common feature of peralkaline rhyolites (see Scaillet & Macdonald, 2001)—preventing the application of 'ilmenite–magnetite' reactions to determine oxygen fugacities (log fO_2) for the rhyolites. Oxygen fugacities were estimated following the formulation of Wones (1981, 1989), based on thermodynamic data for the system titanite–magnetite–quartz. Results range from $-12{\cdot}5$ at 830°C to $\sim -14{\cdot}6$ at 750°C for trachyte and rhyolites, respectively. The trend of oxygen fugacities runs parallel to and above the nickel–nickel oxide (NNO) buffer along a curve roughly defined by FMQ + 1 (where FMQ is the fayalite–magnetite–quartz buffer) with an increase in oxidation towards lower temperatures and more evolved composition (FMQ + 1·2). This is consistent with the single log fO_2 value of -12 at 838°C presented by Crisp & Spera (1987) for ignimbrite 'A', which we infer to be characteristic of the trachyte composition.

Table 3: Combined EMP and SYXRF analyses of feldspar

	Or-poor CR feldspar	Or-rich CR feldspar	Or-rich RF2 feldspar
EMP (wt %)			
SiO_2	67·51	68·48	68·47
TiO_2	0·032	0·02	0·04
Al_2O_3	19·12	18·11	19·3
MgO	0·01	0·03	0·01
CaO	0·1	0·001	0·13
FeO_t	0·9	2·01	0·76
Na_2O	8·05	7·48	7·46
K_2O	3·21	4·36	4·19
Total	98·932	100·491	100·36
Ab	78·8	72·2	72·3
An	0·5	0	0·8
Or	20·7	27·8	26·9
SYXRF (ppm)			
Rb	127	167	31
Ba	3047	2130	583
Nb	2	6·5	0·6
K*	26360	36240	34790
Pb	1·5	2·08	2·02
Sr	18	29	3·9
Zr	27	32	12
Ti	186	155	280
Y	n.d.	n.d.	0·21

*Calculated from EMP analyses.

DISCUSSION

Characteristics and origin of the three endmember magmas

Rhyolite CR appears to have been derived from comenditic trachyte CT by mainly crystal fractionation of oligoclase to anorthoclase feldspar as indicated by major and trace element compositional trends, but neither

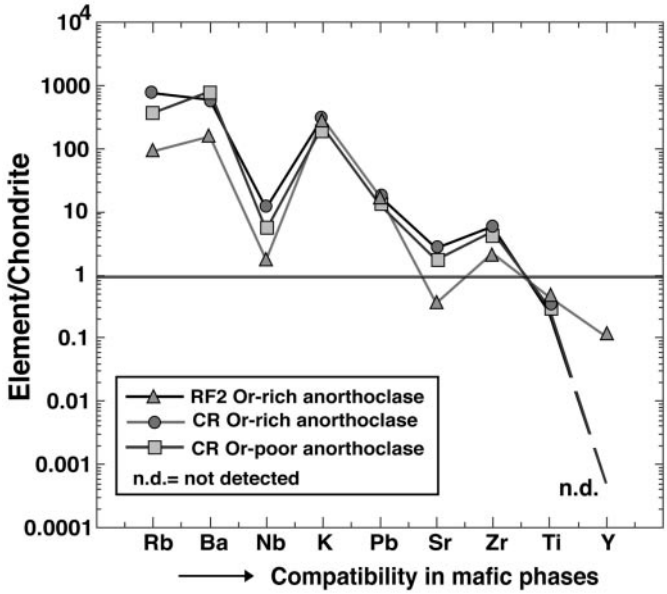

Fig. 12. Multi-element variation plot of trace element spot analyses in feldspars from the two different rhyolitic endmembers analysed by SYXRF. RF2 feldspar is characterized by a depletion in Rb, Ba, Nb, Sr and Zr, and an enrichment in Ti and Y relative to CR feldspars.

appears to be directly linked to rhyolite RF2 by closed-system differentiation. RF2 rhyolite is depleted in incompatible elements relative to rhyolite CR and we interpret rhyolite RF2 as having been selectively contaminated by an evolved Zr- and Nb-poor component during fractionation from a CR rhyolite parent. This contamination is more clearly reflected in incompatible trace elements and REE than in major element concentrations. The interpretation is consistent with the *in situ* feldspar analysis, with RF2 feldspar being characterized by lower concentrations of incompatible elements (Zr, Nb) but higher concentrations of heavy and compatible elements (Ti, Y) relative to CR feldspar crystals. This further supports our interpretation of an input of a distinct component into the RF2 magma, possibly containing some apatite to explain the enrichment in Y.

REE concentrations of feldspar separates show the rhyolite-derived feldspar separates to be generally enriched in REE relative to the trachyte-derived feldspar separates. RF2 feldspar, however, contrasts with CR-derived feldspar in containing distinctly higher HREE, although LREE concentrations are nearly similar. Contamination (i.e. compositional dilution) is therefore most clearly reflected in the *in situ* feldspar and in whole-rock fiamme data. Feldspar separates, on the other hand, resemble a range of crystals from 'early' to 'late' precipitates and thus a mixture of early 'uncontaminated' and late 'contaminated' crystals.

Eu partitioning into feldspar decreases towards more oxidizing conditions (e.g. Wilke & Behrens, 1999) and with decreasing Ca content of the feldspar (e.g. Stix & Gorton 1990). Increasing oxidation and progressive fractionation of the rhyolite magmas would thus have resulted in decreasing concentrations of Eu in the feldspars. Eu concentrations in RF2 feldspar, however, do not substantially differ from Eu concentrations in CT- and CR-derived feldspar. In fact, the feldspar separate from the early fallout tuff (RF2-type feldspar) shows the highest Eu concentrations and CR rhyolite-derived feldspar separates show the lowest Eu concentrations, although conditions were most oxidizing for the RF2 rhyolite ($\log f\mathrm{O}_2 = -14{\cdot}6$ at 750°C). Because RF2 feldspars contain slightly higher Ca contents than CR feldspars (Fig. 5a), we consider the higher Eu concentration in RF2 feldspar to be a function of its Ca content (see Stix & Gorton, 1990). Coupled Eu and Ca partitioning into feldspar may thus have compensated for the increase in oxidation that reduces Eu partitioning by oxidizing Eu^{2+} to Eu^{3+}.

As a consequence of the similarly high Eu concentrations in all feldspar separates, rhyolite magmas of ignimbrite 'A' should have been progressively depleted in Eu by feldspar fractionation. No major negative Eu anomaly was, however, observed in CR and RF2 fiamme, contrasting with the pattern of rhyolites interpreted to have formed by prolonged feldspar removal (compare Freundt & Schmincke, 1995; Civetta *et al.*, 1998). An input of a Eu-bearing component into the rhyolite endmember magmas is thus supported by the near-absence of a negative Eu anomaly in the rhyolites and by the very similar Eu concentrations in feldspar separates of all three

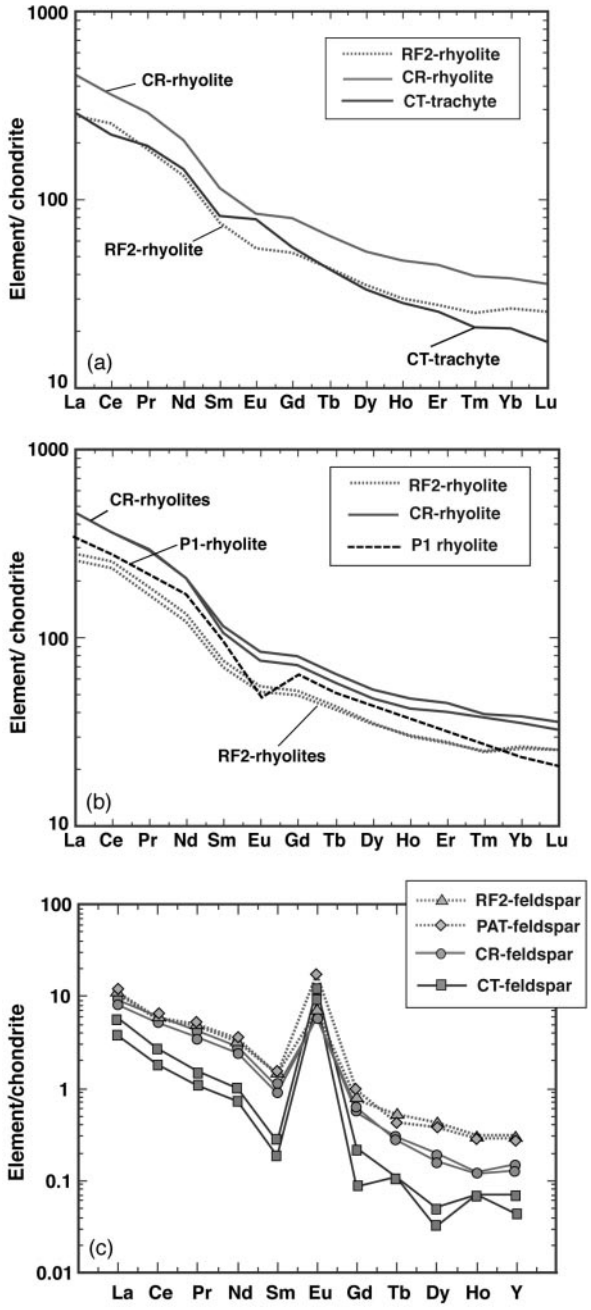

Fig. 13. Chondrite-normalized REE pattern of ignimbrite 'A'. (a) Representative REE pattern of ignimbrite 'A' rhyolites and trachyte. Rhyolite RF2 is strongly depleted in all REE relative to CR rhyolite. The trachyte pattern shows a positive Eu anomaly, reflecting the large abundance of resorbed anorthoclase feldspar in the trachyte samples. (b) REE pattern of two representative CR and two RF2 rhyolite samples plus a reference pattern for a 'P1' rhyolite taken from Freundt & Schmincke (1995). The near-absence of a negative Eu anomaly in CR and RF2 rhyolites compared with the 'P1' rhyolite should be noted. (c) REE pattern of feldspar separates from the three compositional groups including an ignimbrite 'A' fallout sample (PAT). All samples show a strong positive Eu anomaly.

compositional groups, suggesting a feldspar component to the contaminant.

The contrast in FeO_t content between high-iron CR feldspar and RF2 feldspar is probably linked to the occurrence of aegirine–augite in the most evolved RF2 pumices, which is likely to be another consequence of increasing oxidation (compare Bailey, 1969). Aegirine–augite takes up Fe as Fe^{3+}, leaving little Fe^{3+} for the anorthoclase feldspars crystallizing in RF2 (Fe^{3+} is more compatible in anorthoclase than Fe^{2+}). Aegirine–augite is largely lacking in CR type rhyolite, thus permitting high FeO_t contents in some CR feldspars.

Oxygen isotope data for the three feldspar compositional groups contrast with those of previous studies on feldspars from various Mogan units (Crisp & Spera, 1987; Cousens *et al.*, 1993). $\delta^{18}O$ values for ignimbrite 'A' are ~0·4–1·4‰ higher than Crisp & Spera's average of ~6‰ for Mogan feldspars, but only ~0·5‰ higher than the maximum value for 'P1' samples presented by Freundt & Schmincke (1995). Basalt T4 that underlies and pre-dates ignimbrite 'A' shows a $\delta^{18}O$ of 6·1–6·8‰, slightly elevated for a mantle-derived melt expected to display an average value of $\delta^{18}O$ ~5·5–6·0‰ (Garcia *et al.*, 1998). We suspect T4 basalt to have experienced minor contamination in a deep crustal reservoir probably at Moho level, thus raising the $\delta^{18}O$ values by ~0·1–0·8‰. Such contamination by, for example, upper oceanic crust is consistent with the data of Thirlwall *et al.* (1997), Hoernle (1998) and Gurenko *et al.* (2002), who suggested that the shield basalts of Gran Canaria have experienced contamination by interaction with Jurassic ocean crust.

The maximum $\Delta^{18}O_{RF2fsp\text{-}T4basalt}$ yields $\Delta^{18}O$ of 1·19‰, and the maximum $\Delta^{18}O_{CRglass\text{-}T4basalt}$ yields $\Delta^{18}O$ of 2‰. Both values exceed the range of $\Delta^{18}O_{Rhyolite\text{-}Basalt}$ expected for a differentiation series over 20–25 wt % SiO_2 (0·8–1·0‰; Taylor & Sheppard, 1986; Hoefs 1996). The difference between the two rhyolitic feldspar groups is of the order of 0·9‰, for the maximum $\Delta^{18}O_{RF2fsp\text{-}CRfsp}$, although the difference in SiO_2 of the corresponding whole-rock compositions is <5 wt %. Hoefs (1996) suggested a change of ~0·2‰ in $\delta^{18}O$ over 5 wt % SiO_2 during closed-system fractionation, a range clearly exceeded by the $\Delta^{18}O_{RF2fsp\text{-}CRfsp}$. An estimate of the disequilibrium between feldspar and rhyolite melt can be gained by calculation of $\Delta^{18}O_{CRglass\text{-}CRfsp}$, which is found to be of the order of 1·4‰. Crystal melt equilibria are well documented for basalt through rhyolite crystallization sequences by, for example, Taylor & Sheppard (1996), who reported a $\Delta^{18}O_{melt\text{-}fsp}$ of 0·1–0·5‰ to be characteristic for closed-system fractionation in rhyolites. The elevated $\Delta^{18}O_{CRglass\text{-}CRfsp}$ for our samples clearly supports a major crystal–melt disequilibrium between feldspar and melt in the rhyolite magmas of the ignimbrite.

Table 4: REE data of fiamme and feldspar

	CR fiamme			CT fiamme			RF2 fiamme		CR feldspar		CT feldspar		RF2 feldspar	
Sample:	A V F27	A III F28	A IV F35	A III F3	A IV F6	A III F38	A IV F2	A III F11	A IV F32	A IV F36	A III F3	A III F8	PAT-MCA	A III F11
La	142	145	143	103	94·2	90·3	78·9	86·2	2·77	2·47	1·78	1·16	3·22	3·35
Ce	290	304	290	194	177	179	187	205	4·84	4·20	2·13	1·46	4·4	4·71
Pr	35·7	33·7	35·4	26·2	24·1	23·5	20·5	22·4	0·50	0·43	0·19	0·13	0·58	0·61
Nd	124	115	124	98·8	89·5	87·2	72·4	79·6	1·69	1·46	0·60	0·43	1·91	2·03
Sm	20·7	18·8	22·3	17·4	16·3	15·9	13·5	14·7	0·20	0·17	0·05	0·04	0·27	0·27
Eu	5·55	4·97	6·14	5·65	5·66	5·72	3·79	4·07	0·43	0·43	0·87	0·63	1·25	0·51
Gd	18·5	16·6	20·5	15·7	14·9	14·4	12·7	13·5	0·14	0·16	0·06	0·02	0·24	0·19
Tb	2·70	2·26	3·03	2·13	2·06	2·00	1·95	2·04	0·01	0·01	0·01	0·01	0·02	0·02
Dy	15·2	11·9	17·1	11·4	10·7	10·7	11·1	11·3	0·06	0·05	0·02	0·01	0·12	0·13
Ho	3·02	2·24	3·42	2·14	1·98	2·03	2·18	2·15	0·01	0·01	0·01	0·01	0·02	0·02
Er	8·38	5·81	9·45	5·58	5·44	5·32	5·85	5·78	0·02	0·02	<0·01	<0·01	0·07	0·06
Tm	1·21	0·829	1·27	0·741	0·702	0·677	0·796	0·810	<0·005	<0·005	<0·005	<0·005	<0·005	<0·005
Yb	7·37	5·11	8·01	4·43	4·26	4·29	5·36	5·48	<0·01	<0·01	<0·01	<0·01	0·04	0·03
Lu	1·04	0·727	1·14	0·598	0·577	0·563	0·814	0·810	<0·005	<0·005	<0·005	<0·005	0·005	<0·005

Table 5: $\delta^{18}O$ of feldspar and whole rocks

Sample no.	Rock type/description	SiO_2 (wr)	$\delta^{18}O$
PAT-MCa	CR-type fallout tuff	66·96	6·39 (fsp)
PAT-Agu	CR-type fallout tuff	67·95	6·47 (fsp)
A-II-MCa	CR-type flow unit	67·5	6·59 (fsp)
A-F-28	CR-type fiamme	69·44	6·57 (fsp)
A-F-32	CR-type fiamme	68·65	6·68 (fsp)
A-O-MCa	CR-type flow unit	69·22	6·81 (fsp)
A-F-36	CR-type fiamme	69·68	6·96 (fsp)
A-F-27	CR-type fiamme	69·71	7·20 (fsp)
A-F1-BTTS	RF2-type fiamme	70·13	7·11 (fsp)
A-F2-Bto	RF2-type fiamme	70·51	7·25 (fsp)
A-F11-Bto	RF2-type fiamme	70·63	7·32 (fsp)
A-F8	CT-type fiamme	67·59	7·23 (fsp)
A-F3	CT-type fiamme	66·1	7·1 (fsp)
A-F6	CT-type fiamme	66·9	6·83 (fsp)
A-F38	CT-type fiamme	65·89	6·68 (fsp)
A-Pl-1-PR	Syenite fragment in 'A'	59·59	7·11 (wr)
A-Pl-12-PR	Syenite fragment in 'A'	66·92	7·14 (wr)
A-Pl-11-SP	Syenite fragment in 'A'	58·28	7·58 (wr)
T4-MC-1	Alkali-basalt	43·69	6·13 (wr)
T4-MC-2	Alkali-basalt	44·19	6·77 (wr)
T4-PR	Alkali-basalt	43·61	6·79 (wr)
HAFT-3	Hydrothermally altered tuff from caldera margin	65·82	16·23 (wr)
B 913	Jurassic ocean crust* (tholeiitic gabbro, layer 3)	47·55	7·68 (wr)
B 9110	Jurassic ocean crust* (tholeiitic basalt, layer 2)	49·81	8·62 (wr)
HAT 91249	Sedimentary xenolith*† (ocean crust layer 1)	85·57	14·51(wr)
HAT 917 B	Sedimentary xenolith*† (ocean crust layer 1)	87·24	15·48 (wr)

fsp, feldspar; wr, whole rock.
*T. H. Hansteen (unpublished data, 2000).
†Sample of Hoernle (1998).

The evolution from trachyte CT through rhyolite CR to rhyolite RF2 thus appears to be influenced by input of a high $\delta^{18}O$ component at a late stage (Table 5). This happened during crystallization of the feldspar phenocrysts of the RF2 endmember rhyolite and post-dates the major crystallization of feldspar phenocrysts in rhyolite CR. The elevated $\delta^{18}O$ values of the trachyte feldspar separates are best explained by a high percentage of rhyolite-derived feldspar in the trachyte, carrying the high $\delta^{18}O$ signature of their rhyolite parent magma(s). Alternatively, trachyte CT may also have experienced contamination by a distinct component and not only by input of comagmatic feldspar crystals.

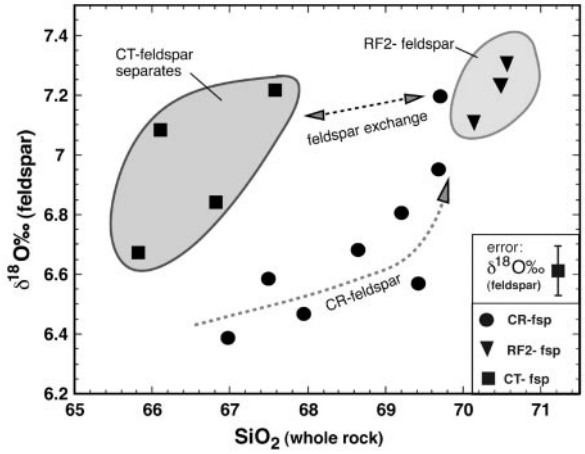

Fig. 14. Whole-rock SiO_2 vs $\delta^{18}O$‰ (feldspar) of ignimbrite 'A' samples. Rhyolite CR shows a strong positive correlation of $\delta^{18}O$‰ with increasing SiO_2 over a narrow range of 4 wt % SiO_2. Rhyolite RF2 shows the highest $\delta^{18}O$‰ values for the given SiO_2 content. Trachyte CT also comprises relatively high $\delta^{18}O$‰ paired with the lowest SiO_2 content. The increase in $\delta^{18}O$‰ for the rhyolite samples with increasing degree of differentiation indicates an input of a heavy oxygen component during differentiation of the CR to the RF2 rhyolite magma. The high oxygen values of the trachyte feldspar separates are consistent with the high concentration of disequilibrium feldspar in CT trachyte samples, supporting crystal exchange between the rhyolite and trachyte magmas.

Combining major elements, trace elements, REE and oxygen isotopes, all three endmember compositions of ignimbrite 'A' appear to have been variably affected by this assimilation depending on their relative position within the magma reservoir. Evidence in trachyte CT comprises resorbed anorthoclase feldspar, elevated feldspar oxygen values as well as a positive Eu anomaly. In CR rhyolite, contamination is manifested in the occurrence of resorbed oligoclase, strongly increasing $\delta^{18}O_{fsp}$ over a limited SiO_2 range as well as the near-absence of a negative Eu anomaly. RF2 rhyolite shows the strongest evidence for contamination including depleted incompatible trace element concentrations, but elevated An, Eu, HREE and $\delta^{18}O$ in feldspar, and the absence of a major negative Eu anomaly in whole rocks.

Possible candidates for a high $\delta^{18}O$ contaminant are: (1) thermally overprinted syenites from the intrusive complex ($\delta^{18}O$ up to 7·6‰); (2) Jurassic igneous ocean crust ($\delta^{18}O$ up to 8·6‰); (3) hydrothermally altered eruptive products of the volcanic pile ($\delta^{18}O$ >15‰); (4) oceanic sediments ($\delta^{18}O$ >14‰). Syenites from the plutonic complex of the island and igneous ocean crust material both have maximum $\delta^{18}O$ values between 7 and 8·6, insufficient for significantly raising the $\delta^{18}O$ values of the contaminated magma, unless assimilation of 50% or more is invoked. Hydrothermally altered tuffs, in turn, have sufficiently high $\delta^{18}O$ values to substantially raise the oxygen value of the contaminated magma by several permil with only a few percent of assimilation,

but they have high Zr, Nb and LREE concentrations, unfavourable for a compositional dilution as observed in rhyolite RF2. Oceanic sediments are very low in incompatible trace element and LREE concentrations, particularly in Nb (6·5 ppm) and Zr (20 ppm) (Hoernle, 1998), and have high $\delta^{18}O$ values (Table 5). Although rigorous trace element modelling is currently impossible, as the effects of, for example, chevkinite crystallization are poorly constrained, the component that qualitatively satisfies high $\delta^{18}O$ and low incompatible trace element and LREE concentrations is oceanic sediment. A further argument in favour of oceanic sediments is their high water content and their siliciclastic nature, implying that a rhyolite magma with a temperature of 750–770°C is sufficiently hot to melt such a rock. A first estimate on the basis of oxygen isotopes yields ~8–10% sediment-derived oxygen in RF2 feldspar and ~20% of sediment-derived oxygen in the rhyolite glass. A more detailed quantification of the assimilation rate including radiogenic isotopes is in progress and will be presented elsewhere.

Feldspar petrography and compositional zoning

We showed that the three compositional groups of ignimbrite 'A' also crystallized three distinct feldspar compositions, which allow us to trace an individual composition back to the magma from which it crystallized. The relative abundance of anorthoclase (rhyolite) to oligoclase (trachyte) feldspar, based on ~1000 EMP spot-analyses, displays a dominance of anorthoclase in the ignimbrite, although, as mentioned above, crystal content in the trachyte is highest (Fig. 7). Up to 45% of the feldspar population in the trachyte is strongly resorbed anorthoclase that originally crystallized in the rhyolite(s). RF2 rhyolite lacks resorbed crystals and contains only small euhedral anorthoclase. CR rhyolite contains a small proportion of resorbed crystals of mainly oligoclase composition. The high proportion of feldspar in CT trachyte relative to the rhyolites, combined with the high percentage of resorbed anorthoclase crystals in CT, suggests that crystal settling was an important process in the redistribution of phenocrysts within the magma chamber (compare Table 2a). On the other hand, partially resorbed oligoclase crystals in CR rhyolite emphasize that exchange of crystals was also accomplished the other way round, that is, by uprise from trachyte into rhyolite. This was, however, less effective than the general tendency for crystals to move to lower stratigraphic levels in the magma chamber. Physical mingling of the different magmas as well as small-scale uprise of vesiculated batches across transitional interfaces appears plausible, especially when taking vesiculation, crystal accumulation from above, volatile accumulation from underneath as well as pressure shadows and shear forces into account. Such processes are likely to cause local density inversions, leading to intimate mixing of the magmas (e.g. Eichelberger, 1980; Turner *et al.*, 1982).

Several distinct zoning types can be expected in crystals that grew in such a magma system, depending on their particular place of formation and travel path throughout the magma chamber. Crystals with normal zoning are thought to have formed by diffusion-controlled growth, crystallizing in one of the endmember magmas exclusively throughout their entire magmatic lifespan. Some feldspar crystals may well have formed in a mushy crystallization zone at the margins of the chamber where cooling is most effective and crystals tend to be locked in advancing solidification fronts but are still in continuous contact with the percolating melt (see Marsh, 1996). Reverse zoning requires changes towards either higher pressure or temperature, or a more mafic melt composition. As the latter would produce far stronger compositional differences (i.e. >10 mol % Ab and Or) and less gradual zoning pattern, we infer that the reversely zoned feldspars are the result of small pressure and temperature changes. This may be accomplished by either crystal settling, where crystals settle into deeper regions of the same liquid body to experience minor increase in pressure and temperature, or convection within an individual liquid body. The latter process is physically likely, considering that peralkaline felsic melts are generally less viscous than evolved calc-alkaline magmas (Hess *et al.*, 1995). Both normal and reverse zoned crystals are clearly oscillatory in their small-amplitude variation probably as a result of minor local disequilibrium or small-scale pressure and temperature changes (Loomis, 1982; Pearce & Kolisnik, 1990; Pearce, 1994). They nevertheless represent growth in a fairly homogeneous chemical and physical environment relative to the complexly zoned crystal types. A far more complex scenario, including magma mixing, appears to be required to account for those crystals with type III and IV zoning pattern. A plausible model needs to incorporate at least two magmas (e.g. trachyte and rhyolite), which mutually exchanged magma batches and the crystals contained within them. This has to include crystals grown in either endmember liquid subsequently released into the other endmember and transferred back to their parent liquid by various fluid dynamic processes. A possible sequence of events is illustrated in Fig. 15. The individual steps are summarized as follows:

(1) feldspar crystal growth in endmember magma (i.e. rhyolite);

(2) viscous entrainment of a rhyolite batch along, for example, rhyolite–trachyte interface;

(3) mixing of rhyolite into trachyte places the rhyolitic feldspar in the trachyte melt;

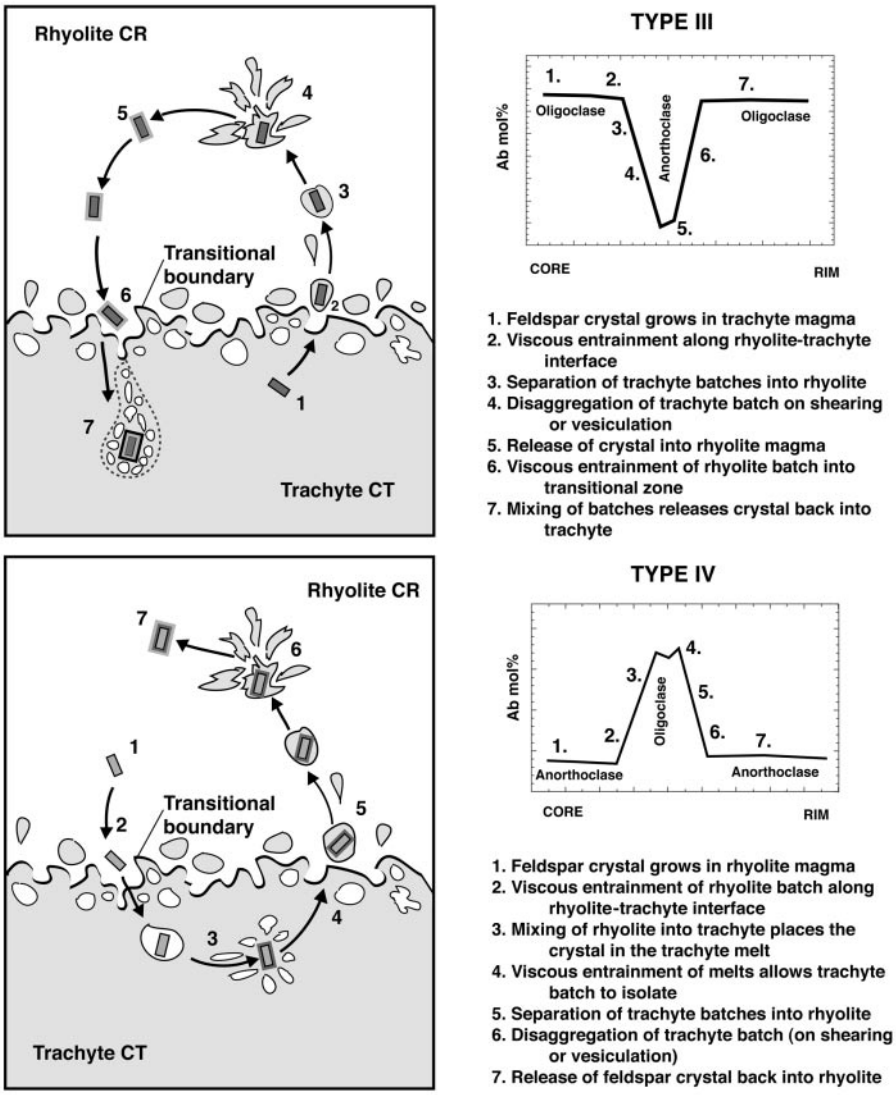

Fig. 15. Step-cycle model for type III and type IV feldspar zonations.

(4) resorption of rhyolitic feldspar followed by overgrowth with a trachyte feldspar composition;

(5) viscous entrainment of melt batches along rhyolite–trachyte interface allows trachyte batch to isolate;

(6) trachyte batch segregates and rises into the rhyolite melt body by either volatile exsolution (see Eichelberger, 1980) or convection within the rhyolite forced upon the trachyte batch;

(7) disaggregation of the trachyte batch (on shearing or vesiculation) releases feldspar crystals back into the rhyolite melt, where they are overgrown by a rhyolitic feldspar composition.

This 'step-cycle model' elaborates on the ideas of Tepley *et al.* (1999), where crystals are transferred between distinct magma batches. Our model differs, however, in that magma mixing was not by mafic recharge of the felsic chamber of ignimbrite 'A' but by small-scale mixing of several genetically linked magmas of different composition. The crystal exchange model is consistent with single crystals showing one or more complete cycles and other crystals that show incomplete cycles, owing to the interruption of the travel path by eruption or the trapping of crystals in one of the endmember magmas (compare Fig. 9b). This mode of crystal exchange provides strong support for contemporaneous residence of several magmas in a single reservoir, sufficiently long to allow for crystal transfer, resorption and overgrowth to take place, contrasting with the view of Eichelberger *et al.* (2000), who suggested that distinct magma compositions

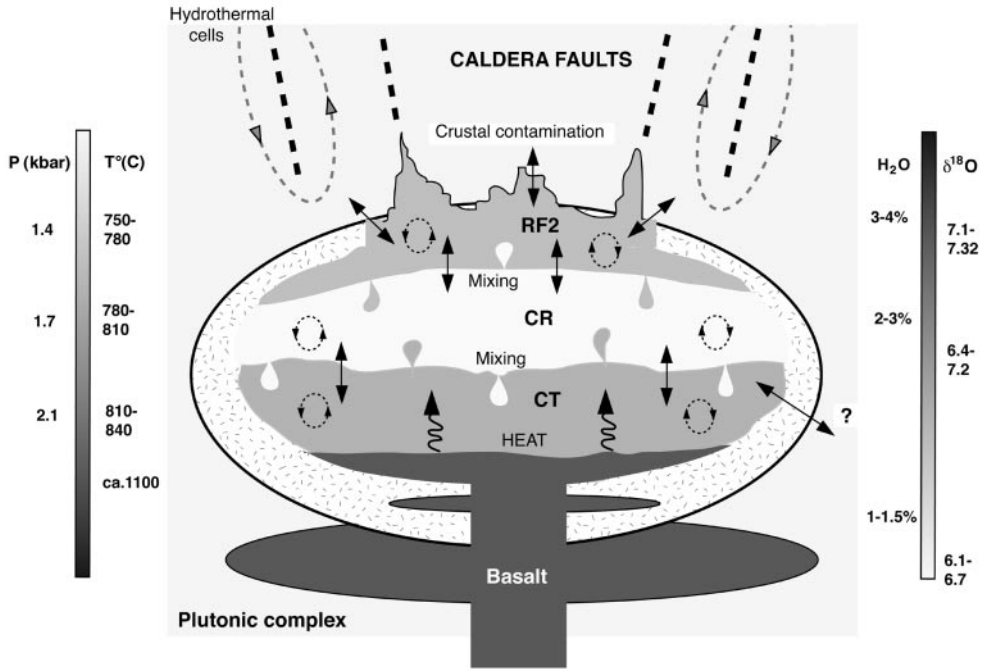

Fig. 16. Model of chemical and physical gradients in the ignimbrite 'A' magma chamber. The zonation of the chamber comprises basalt in the lowermost parts of the chamber, progressively overlain by trachyte and the two rhyolite magmas. A compositional gap between basalt and trachyte is shown in the sketch but is not thought to imply the entire absence of intermediate compositions. Contamination was strongest in the upper parts of the system, where cooling was most effective. The trachyte magma and the two rhyolite magmas are shown to have mixed by small convective plumes to achieve mutual crystal exchange. Internal magma layer convection is indicated in the drawing, and is thought to reflect the conditions that produced normal and reversely zoned feldspar.

of zoned ignimbrites may have 'first met' just before eruption. A summary scenario of the magma chamber on the basis of the geochemical and *P*, *T* data is shown in Fig. 16.

The model also implies that ternary feldspar is able to record magma chamber processes in peralkaline systems, conceptually similar to plagioclase in calc-alkaline systems, although using albite (Ab) and orthoclase (Or) as the sensitive parameters. Pearce & Kolisnik (1990) distinguished two types of compositional zoning in plagioclase: (1) type I, showing zones with small compositional amplitudes lacking internal dissolution surfaces, characteristic for diffusion-controlled 'near-equilibrium' growth; (2) type II, characterized by large compositional amplitudes and usually associated with one or more dissolution event(s). The second type is thought to be controlled by melt composition and indicates severe chemical changes in the crystallization environment (i.e. magma mixing). Analogous to the two zonation types of Pearce & Kolisnik (1990), normal and reverse zoning of this study is represented by Pearce & Kolisnik's type I zoning, whereas complex zoning in ignimbrite 'A' feldspar follows their type II zoning pattern.

CONCLUSION

Ternary feldspar in ignimbrite 'A' reveals the complex record of crystallization conditions and processes that the host magmas were subjected to. Besides fractional crystallization, feldspar crystals also record evidence for convective magma movements, magma mixing and crustal assimilation in a shallow-level magma reservoir. We suggest that crystal settling and small-scale convection were important processes in the ignimbrite 'A' magma chamber, allowing for mutual crystal exchange between the various compositional groups. Crystal transfer followed a step cycle, with each step being reflected in the zoning pattern of complexly zoned crystals. Ternary feldspars thus record magmatic processes just as well as plagioclase and sanidine involving albite and orthoclase as the sensitive parameters. This is especially relevant to evolved peralkaline rocks where ternary feldspar is the dominant phenocryst phase and plagioclase is scarce or absent.

Fractional crystallization from a trachyte parent appears to be an important process in generating rhyolitic magmas on Gran Canaria, but crustal recycling commonly modifies evolved magmas on differentiation.

Crustal contamination, as recorded in the phenocrysts of ignimbrite 'A', may be a more important process in the generation of felsic ocean island magmas than previously thought.

ACKNOWLEDGEMENTS

Drs P. M. Sachs and F. Lechtenberg are thanked for assistance with SYXRF analyses, O. Schneider and D. Rau for assistance with the EMS and XRF facilities at GEOMAR, and C. Harris, J. Hoefs and A. Gurenko for oxygen isotope analyses. K. Hoernle and T. H. Hansteen kindly provided samples of ocean crust xenoliths. We are also grateful to T. H. Hansteen and A. Freundt for discussion, and to A. Gurenko and M. Hort for constructive criticism on earlier versions of the manuscript. We thank F. J. Tepley III, J. A. Wolff and two anonymous reviewers for thought-provoking reviews, and G. Bergantz for editorial handling. Financial support by the 'Deutsche Forschungsgemeinschaft' (Grant Schm 250/72-1 to H.U.S.) and a stipend to V.R.T. by the 'Studienstiftung des deutschen Volkes' are gratefully acknowledged.

REFERENCES

Anderson, J. L. & Smith, D. R. (1995). The effect of temperature and oxygen fugacity on Al-in-hornblende barometry. *American Mineralogist* **80**, 549–559.

Bailey, D. K. (1969). The stability of acmite in the presence of H_2O. *American Journal of Science* **267**, 1–16.

Blake, S. (1981). Eruptions from zoned magma chambers. *Journal of the Geological Society, London* **138**, 281–287.

Blundy, J. D. & Shimizu, N. (1991). Trace element evidence for plagioclase recycling in calc-alkaline magmas. *Earth and Planetary Science Letters* **102**, 178–197.

Bogaard, P. van den & Schmincke, H.-U. (1998). Chronostratigraphy of Gran Canaria. In: Weaver, P. P. E., Schmincke, H.-U., Firth, J. V. & Duffield, W. (eds) *Proceedings of the Ocean Drilling Program, Scientific Results 157*. College Station, TX: Ocean Drilling Program, pp. 127–140.

Borthwick, J. & Harmon, R. S. (1982). A note regarding ClF_3 as an alternative to BrF_5 for oxygen isotope analysis. *Geochimica et Cosmochimica Acta* **46**, 1665–1668.

Brophy, J. G., Dorais, M. J., Donnelly-Nolan, J. & Singer, B. S. (1996). Plagioclase zoning styles in hornblende gabbro inclusions from Little Glass Mountain, Medicine Lake volcano, California: implications for fractionation mechanisms and the formation of composition gaps. *Contributions to Mineralogy and Petrology* **126**, 121–136.

Carmichael, I. S. E. & MacKenzie, W. S. (1963). Feldspar–liquid equilibria in pantellerites: an experimental study. *American Journal of Science* **261**, 382–396.

Civetta, L., Dántonino, M., Orsi, G. & Tilton, G. R. (1998). The geochemistry of volcanic rocks from Pantelleria Island, Sicily Channel: petrogenesis and characteristics of the mantle source region. *Journal of Petrology* **39**, 1453–1491.

Cousens, B. L., Spera, F. J. & Tilton, G. R. (1990). Isotopic patterns in silicic ignimbrites and lava flows of the Mogan and the lower Fataga Formations, Gran Canaria, Canary Islands: temporal changes in mantle source composition. *Earth and Planetary Science Letters* **96**, 319–335.

Cousens, B. L., Spera, F. J. & Dobson, P. F. (1993). Post eruptive alteration of silicic ignimbrites and lavas, Gran Canaria, Canary Islands: strontium, neodymium, lead and oxygen isotopic evidence. *Geochimica et Cosmochimica Acta* **57**, 631–640.

Crisp, J. A. & Spera, F. J. (1987). Pyroclastic flows and lavas of the Mogan and Fataga formations, Tejeda volcano, Gran Canaria, Canary Islands: mineral chemistry, intensive parameters, and magma chamber evolution. *Contributions to Mineralogy and Petrology* **96**, 503–518.

Davidson, J. P. & Tepley, F. J., III (1997). Recharge in volcanic systems; evidence from isotope profiles of phenocrysts. *Science* **275**, 826–829.

Davidson, J. P., Tepley, F. J., III, Palacz, Z. & Main, S. (2001). Magma recharge, contamination and residence times revealed by *in situ* laser ablation isotopic analysis of feldspar in volcanic rocks. *Earth and Planetary Science Letters* **182**, 427–442.

Devine, J. D., Gardner, J. E., Brack, H. P., Layne, G. D. & Rutherford, M. J. (1995). Comparison of microanalytical methods for estimating H_2O contents of silicic volcanic glasses. *American Mineralogist* **80**, 319–328.

Eichelberger, J. C. (1980). Vesiculation of mafic magmas during replenishment of silicic magma reservoirs. *Nature* **288**, 446–450.

Eichelberger, J. C., Chertkoff, D. G., Dreher, S. T. & Nye, C. J. (2000). Magmas in collision: rethinking chemical zonation in silicic magmas. *Geology* **28**, 603–606.

Freundt, A. & Schmincke, H.-U. (1995). Petrogenesis of rhyolite–trachyte–basalt composite ignimbrite P1, Gran Canaria, Canary Islands. *Journal of Geophysical Research* **100**, 455–474.

Freundt-Malecha, B. (1997). The crystallized portions of magmatic systems exposed by mafic through felsic plutonic fragments in ignimbrites on Gran Canaria. Ph.D. thesis, Christian-Albrechts-Universität, Kiel, 208 pp.

Freundt-Malecha, B., Schmincke, H.-U. & Freundt, A. (2001). Plutonic rocks of intermediate composition on Gran Canaria: the missing link of the bimodal volcanic rock suite. *Contributions to Mineralogy and Petrology* **141**, 430–455.

Garbe-Schönberg, C. D. (1993). Simultaneous determination of thirty-seven trace elements in twenty-eight international rock standards by ICP-MS. *Geostandards Newsletter* **17**, 81–97.

Garcia, M. O., Ito, E., Eiler, J. M. & Pietruszka, A. J. (1998). Crustal contamination of Kilauea Volcano magmas revealed by oxygen isotope analyses of glass and olivine from Pùu Oò eruption lavas. *Journal of Petrology* **39**, 803–817.

Grove, T. L., Kinzler, R. J. & Bartels, K. S. (1989). Effects of pressure on alumina substitution in igneous augite: an empirical barometer. *EOS Transactions, American Geophysical Union* **70**, 1401–1402.

Gurenko, A., Chaussidon, M. & Schmincke, H.-U. (2002). S and O isotopic composition of cpx-hosted glass inclusions from Miocene basaltic hyaloclastites of Gran Canaria (ODP Leg 157): an ion microprobe study. *Geochimica et Cosmochimica Acta* (in press).

Hansteen, T. H., Sachs, P. M. & Lechtenberg, F. (2000). Synchrotron-XRF microprobe analysis of silicate reference standards using fundamental parameter quantification. *European Journal of Mineralogy* **12**, 25–31.

Harris, C., Smith, H. S. & le Roex, A. (2000). Oxygen isotope composition of phenocrysts from Tristan da Cunha and Gough Island lavas: variation with fractional crystallization and evidence for assimilation. *Contributions to Mineralogy and Petrology* **138**, 164–175.

Helz, R. T. (1979). Alkali exchange between hornblende and melt: a temperature sensitive reaction. *American Mineralogist* **64**, 593–665.

Hess, K.-U., Dingwell, D. B. & Webb, S. L. (1995). The influence of excess alkalis on the viscosity of a haplogranitic melt. *American Mineralogist* **80**, 297–304.

Hoefs, J. (1996). *Stable Isotope Geochemistry*. Berlin: Springer, 201 pp.

Hoernle, K. (1998). Geochemistry of Jurassic ocean crust beneath Gran Canaria (Canary Islands): implications for crustal recycling and assimilation. *Journal of Petrology* **39**, 859–880.

Hoernle, K. & Schmincke, H.-U. (1993). The role of partial melting in the 15 Ma geochemical evolution of Gran Canaria: a blob model for the Canary hotspot. *Journal of Petrology* **34**, 599–626.

Janssens, K., Vincze, L., van Espen, P. & Adams, F. (1993). Monte Carlo simulation of conventional and synchrotron energy dispersive X-ray spectrometers. *X-ray Spectrometry* **22**, 234–243.

Johnson, M. C. & Rutherford, M. J. (1989). Experimental calibration of the aluminum-in-hornblende geobarometer with application to the Long Valley caldera (California) volcanic rocks. *Geology* **17**, 837–841.

Knesel, K. M., Davidson, J. P. & Duffield, W. A. (1999). Evolution of silicic magma through assimilation and subsequent recharge: evidence from Sr isotopes in sanidine phenocrysts, Taylor Creek rhyolite, NM. *Journal of Petrology* **40**, 773–786.

Krastel, S. & Schmincke, H.-U. (2002). Crustal structure of northern Gran Canaria deduced from active seismic tomography. *Journal of Geophysical Research* (in press).

Lechtenberg, F., Garbe, S., Bauch, J., Dingwell, D. B., Freitag, J., Haller, M., Hansteen, T. H., Knöchel, A., Radtke, M., Romano, C., Sachs, P. M., Schmincke, H.-U. & Ullrich, H. J. (1996). The X-ray fluorescence measurement place at beamline L of HASYLAB. *Journal of Trace and Microprobe Techniques* **14**, 561–587.

Lofgren, G. (1980). Experimental studies on the dynamic crystallisation of silicate melts. In: Hargraves, R. B. (ed.) *Physics of Magmatic Processes*. Princeton, NJ: Princeton University Press, pp. 478–551.

Loomis, T. P. (1982). Numerical simulations of crystallisation processes of plagioclase in complex melts. The origin of major and oscillatory zoning in plagioclase. *Contributions to Mineralogy and Petrology* **81**, 219–229.

Macdonald, R. (1974). Nomenclature and petrochemistry of the peralkaline oversaturated extrusive rocks. *Bulletin of Volcanology* **38**, 498–516.

Marsh, B. D. (1996). Solidification fronts and magmatic evolution. *Mineralogical Magazine* **60**, 5–40.

Naney, M. T. (1983). Phase equilibria of rock-forming ferromagnesian silicates in granitic systems. *American Journal of Science* **283**, 993–1033.

Nekvasil, H. (1994). Ternary feldspar/melt equilibria: a review. In: Parsons, I. (ed.) *Feldspars and their Reactions*. Dordrecht: Kluwer Academic, pp. 195–219.

Nekvasil, H., Simon, A. & Lindsley, D. H. (2000). Crystal fractionation and the evolution of intra-plate hy-normative igneous suites: insights from their feldspars. *Journal of Petrology* **41**, 1743–1757.

Nielsen, C. H. & Sigurdsson, H. (1981). Quantitative methods for electron microprobe analysis of sodium in natural and synthetic glasses. *American Mineralogist* **66**, 547–552.

Pearce, T. H. (1994). Recent work on oscillatory zoning in plagioclase. In: Parsons, I. (ed.) *Feldspars and their Reactions*. Dordrecht: Kluwer Academic, pp. 313–349.

Pearce, T. H. & Kolisnik, A. M. (1990). Observations of plagioclase zoning using interference imaging. *Earth-Science Reviews* **29**, 9–26.

Pouchou, J. L. & Pichoir, F. (1984). A new model for quantitative X-ray microanalysis, Part I. Application to the analysis of homogeneous samples. *Recherche Aerospatiale* **3**, 13–38.

Rona, P. A., Brakl, J. & Heitzler, J. R. (1970). Magnetic anomalies in the Northeast Atlantic between the Canary and Cape Verde Islands. *Journal of Geophysical Research* **75**, 7412–7420.

Sachs, P. M. & Hansteen, T. H. (2000). Pleistocene underplating and metasomatism of the lower continental crust: a xenolith study. *Journal of Petrology* **41**, 331–356.

Scaillet, B. & Macdonald, R. (2001). Phase relations of peralkaline silicic magmas and petrogenetic implications. *Journal of Petrology* **42**, 825–845.

Schirnick, C., Bogaard, P. v. d. & Schmincke, H.-U. (1999). Cone sheet formation and intrusive growth of an oceanic island—the Miocene Tejeda complex on Gran Canaria (Canary Islands). *Geology* **27**, 207–210.

Schmincke, H.-U. (1969). Petrologie der phonolitischen bis rhyolitischen Vulkanite auf Gran Canaria, Kanarische Inseln. Habilitationsschrift, Universität Heidelberg, 151 pp.

Schmincke, H.-U. (1976). The geology of the Canary Islands. In: Kunkel, G. (ed.) *Biogeography and Ecology in the Canary Islands*. The Hague: W. Junk, pp. 67–184.

Schmincke, H.-U. (1994). *Geological Gield Guide of Gran Canaria: Part I and II*. Witten: Pluto Press, pp. 1–64.

Schmincke, H.-U., Klügel, A., Hansteen, T. H., Hoernle, K. & Bogaard, P. v. d. (1998). Samples from the Jurassic ocean crust beneath Gran Canaria, La Palma and Lanzarote (Canary Islands). *Earth and Planetary Science Letters* **163**, 343–360.

Silver, L. A., Ihinger, P. D. & Stolper, E. (1990). The influence of bulk composition on the speciation of water in silicate glasses. *Contributions to Mineralogy and Petrology* **104**, 142–162.

Singer, B. S., Dingan, M. A. & Layne, G. D. (1995). Textures and Sr, Ba, Mg, Fe, K, and Ti compositional profiles in volcanic plagioclase: clues to the dynamics of calc-alkaline magma chambers. *American Mineralogist* **80**, 776–798.

Stamatelopoulou-Seymore, K., Vlassopoulos, D., Pearce, T. & Rice, C. (1990). The record of magma chamber processes in plagioclase phenocrysts at the Thera volcano, Aegean volcanic arc, Greece. *Contributions to Mineralogy and Petrology* **104**, 73–84.

Stewart, M. L. & Fowler, A. D. (2001). The nature and occurrence of discrete zoning in plagioclase from recently erupted andesitic volcanic rocks, Montserrat. *Journal of Volcanology and Geothermal Research* **106**, 243–253.

Stix, J. & Gorton, M. P. (1990). Variations in trace element partition coefficients in sanidine in the Cerro Toledo rhyolite, Jemez Mountains, New Mexico: effects of composition, temperature and volatiles. *Geochimica et Cosmochimica Acta* **54**, 2697–2708.

Sumita, M. & Schmincke, H.-U. (1998). Tephra event stratigraphy and emplacement of volcaniclastic sediments, Mogan and Fataga stratigraphic intervals, Part I: mineral and chemical stratigraphy of volcaniclastic units and correlation to the subaerial record. In: Weaver, P. P. E., Schmincke, H.-U., Firth, J. V. & Duffield, W. (eds) *Proceedings of the Ocean Drilling Program, Scientific Results 157*. College Station, TX: Ocean Drilling Program, pp. 219–266.

Taylor, H. P. & Sheppard, S. M. F. (1986). Igneous rocks: I. Processes of isotopic fractionation and isotope systematics. In: Valley, J. W., Taylor, H. P., Jr & O'Neil, J. R. (eds) *Stable Isotopes. Mineralogical Society of America, Reviews in Mineralogy* **16**, 227–271.

Tepley, F. J., III, Davidson, J. P. & Clynne, M. A. (1999). Magmatic interactions as recorded in plagioclase phenocrysts of Chaos Crags, Lassen Volcanic Center, California. *Journal of Petrology* **40**, 787–806.

Thirlwall, M. F., Jenkins, C., Vroon, P. C. & Mattey, D. P. (1997). Crustal interaction during construction of oceanic islands: Pb–Sr–Nd and O isotope stratigraphy of the shield basalts of Gran Canaria. *Chemical Geology* **135**, 233–262.

Thomas, R. (1990). Abschätzung der Bildungstemperatur magmatischer Schmelzen. *Zeitschrift der Geologischen Wissenschaften* **18**, 5–14.

Troll, V. R., Sachs, P. M. & Schmincke, H.-U. (1999). Trace element concentrations in alkali-feldspar from peralkaline ash-flow 'A', Gran Canaria: tracing magmatic processes. *HASYLAB Annual Report 1999*. Hamburg: Hamburger Synchrotronstrahlungslabor HASYLAB am Deutschen Elektronensynchrotron DESY, pp. 1001–1002.

Tsuchiyama, A. (1985). Dissolution kinetics of plagioclase in the melt of the system diopside–albite–anorthite, and the origin of dusty plagioclase in andesites. *Contributions to Mineralogy and Petrology* **89**, 1–16.

Turner, J. S., Huppert, H. E. & Sparks, R. S. J. (1982). An experimental investigation of volatile exsolution in evolving magma chambers. *Journal of Volcanology and Geothermal Research* **16**, 263–277.

Tuttle, O. F. & Bowen, N. L. (1958). Origin of granite in the light of experimental studies in the system $NaAlSi_3O_8$–$KAlSi_3O_8$–SiO_2–H_2O. *Geological Society of America, Memoirs* **74**, 1–153.

van Wagoner, N. A., Leybourne, M. I., Pearce, T. H. & Timms, C. E. (1995). Comparison of petrogenetic processes between the West Valley segment of Juan de Fuca Ridge and the adjacant Heck Chain of seamounts: detailed electron microprobe study and Nomarski interference imaging of plagioclase. *Canadian Mineralogist* **33**, 569–583.

Vincze, L., Janssens, K. & Adams, F. (1993). A general Monte Carlo simulation of energy dispersive X-ray fluorescence spectrometers—Part I. *Spectrochimica Acta* **48**, 553–573.

Wilke, M. & Behrens, H. (1999). The dependence of the partitioning of iron and europium between plagioclase and hydrous tonalitic melt on oxygen fugacity. *Contributions to Mineralogy and Petrology* **137**, 102–114.

Wones, D. R. (1981). Biotites and amphiboles in igneous rocks: dehydration redox reactions. In: Veblen, D. R. & Ribbe, P. H. (eds) *Amphiboles: Petrology and Experimental Phase Relations. Mineralogical Society of America, Reviews in Mineralogy* **9B**, 357–371.

Wones, D. R. (1989). Significance of the assemblage titanite + magnetite + quartz in granitic rocks. *American Mineralogist* **74**, 744–749.

APPENDIX

Table A1: Representative chemical analysis of matrix-glass, melt inclusions and amphiboles

	Trachyte matrix-glass			Trachytic melt inclusions			Amphiboles in trachyte		
SiO_2	65·29	65·35	66·61	62·68	63·6	65·04	49·86	49·96	50·04
TiO_2	0·90	0·94	0·83	1·01	1·13	0·63	2·51	1·94	1·94
Al_2O_3	15·27	15·78	15·37	15·73	15·64	15·23	4·25	4·53	4·51
FeO_t	3·56	3·59	3·35	3·93	3·79	3·52	11·54	10·42	10·30
MnO	0·21	0·21	0·18	0·26	0·18	0·27	1·35	1·25	1·32
MgO	0·91	0·71	0·85	1·08	0·55	0·75	16·01	16·62	16·82
CaO	1·40	1·43	1·24	1·77	1·22	1·09	7·91	8·12	8·09
Na_2O	6·97	7·07	7·24	6·76	6·65	7·14	4·75	4·88	4·90
K_2O	4·22	4·31	4·040	3·68	3·78	4·01	0·84	0·77	0·74
P_2O_5	0·33	0·31	0·18	0·89	0·82	0·22	0·12	0·11	0·11
F	0·11	0·12	0·092	0·22	0·15	0·11	1·01	1·18	1·23
Cl	0·12	0·018	0·00	0·075	0·058	0·031	0·003	0·029	0·017
Total	99·29	99·84	99·98	98·09	97·57	98·04	100·16	99·81	100·02
	Rhyolite matrix-glass			Rhyolitic melt inclusions			Amphiboles in rhyolite		
SiO_2	69·76	70·77	71·03	67·71	68·21	69·03	52·85	52·63	52·34
TiO_2	0·72	0·51	0·51	0·67	1·31	0·62	1·59	1·45	1·57
Al_2O_3	12·63	12·73	12·72	12·34	12·15	12·18	2·49	2·25	2·41
FeO_t	3·69	3·14	3·24	3·67	3·68	3·42	10·4	11·15	10·63
MnO	0·24	0·18	0·15	0·31	0·12	0·34	1·37	1·52	1·44
MgO	0·47	0·31	0·26	0·38	0·11	0·31	16·80	16·91	17·11
CaO	0·14	0·087	0·086	0·19	0·13	0·28	6·88	6·62	6·82
Na_2O	6·35	5·91	5·93	5·99	6·26	6·14	5·14	5·31	5·5
K_2O	4·53	4·61	4·63	4·65	4·38	4·66	0·83	0·93	0·84
P_2O_5	0·032	0·045	0·096	0·07	0·02	0·048	0·082	0·099	0·073
F	0·044	0·096	0·21	0·33	0·085	0·078	1·20	1·14	1·17
Cl	0·053	0·26	0·18	0·17	0·046	0·052	0·037	0·032	0·015
Total	98·66	98·65	99·04	96·48	96·50	97·16	99·66	100·04	99·92